

2

AD-A232 383

PAGE

Form Approved
OMB No. 0704-0188

Public domain
gathering and
collection of
Davis Highway

Responsibility including the time for reviewing instructions, searching existing data sources, gathering additional information, sending comments regarding this burden estimate or any other aspect of this collection of information, including suggestions for reducing this burden, to Washington Headquarters Services, Directorate for Information Operations and Reports, 1215 Jefferson Davis Highway, Suite 1204, Arlington, VA 22202-4302, and to the Office of Management and Budget, Paperwork Reduction Project (0704-0188), Washington, DC 20503

1. AGENCY (Leave blank)		2. REPORT DATE 5 May 1989	3. REPORT TYPE AND DATES COVERED TECHNICAL REPORT	
4. TITLE AND SUBTITLE STUDY OF SURFACE PHENOMENA IN CERAMICS BY TEM			5. FUNDING NUMBERS DAAL03-87-K-0104	
6. AUTHOR(S) David W. Susnitzky and C. Barry Carter			8. PERFORMING ORGANIZATION REPORT NUMBER MAR 1 1989	
7. PERFORMING ORGANIZATION NAME(S) AND ADDRESS(ES) MATERIALS SCIENCE & ENGINEERING DEPT. CORNELL UNIVERSITY ITHACA, NY14853-1501			10. SPONSORING / MONITORING AGENCY REPORT NUMBER ARO 24417.17-EL	
9. SPONSORING / MONITORING AGENCY NAME(S) AND ADDRESS(ES) U. S. Army Research Office P. O. Box 12211 Research Triangle Park, NC 27709-2211				
11. SUPPLEMENTARY NOTES The view, opinions and/or findings contained in this report are those of the author(s) and should not be construed as an official Department of the Army position, policy, or decision, unless so designated by other documentation.				
12a. DISTRIBUTION / AVAILABILITY STATEMENT Approved for public release; distribution unlimited.			12b. DISTRIBUTION CODE	
13. ABSTRACT (Maximum 200 words) The use of transmission electron microscopy for the study of a range of phenomena associated with the surfaces of ceramic materials is discussed. The approach used throughout the work described has been to prepare a thinned sample in a form suitable for imaging in the electron microscopy and then to modify the characteristics of this sample by heat treating it. The same sample is then used for further studies by depositing metallic or ceramic particles on the surface. The material systems illustrated include SiC and Al ₂ O ₃ as the thin film with the particles being Cu, W, ThO ₂ or NiO.				
14. SUBJECT TERMS ELECTRONIC PACKAGING, SURFACE AND INTERFACES			15. NUMBER OF PAGES 48	
			16. PRICE CODE	
17. SECURITY CLASSIFICATION OF REPORT UNCLASSIFIED	18. SECURITY CLASSIFICATION OF THIS PAGE UNCLASSIFIED	19. SECURITY CLASSIFICATION OF ABSTRACT UNCLASSIFIED	20. LIMITATION OF ABSTRACT UL	

STUDY OF SURFACE PHENOMENA IN CERAMICS BY TEM+

David W. Susnitzky and C. Barry Carter

Department of Materials Science and Engineering,
Cornell University,
Ithaca, NY 14853

Report No. P002

issued by

The Materials Science Center
Cornell University

5 May, 1989

All correspondence should be addressed to: Prof. C. Barry Carter at Cornell

91 2 15 058

Abstract

The use of transmission electron microscopy for the study of a range of phenomena associated with the surfaces of ceramic materials is discussed. The approach used throughout the work described has been to prepare a thinned sample in a form suitable for imaging in the electron microscopy and then to modify the characteristics of this sample by heat treating it. The same sample is then used for further studies by depositing metallic or ceramic particles on the surface. The material systems illustrated include SiC and Al₂O₃ as the thin film with the particles being Cu, W, ThO₂ or NiO.

Accession For	
NTIS GRA&I	<input checked="" type="checkbox"/>
ETD	<input type="checkbox"/>
Unannounced	<input type="checkbox"/>
Justification	
By	
Date Recd	
Availability Codes	
Dist	Availability for Special
A-1	



+ Paper presented in the Symposium on "Interfaces in Ceramic Materials" at the Fall Meeting of the American Ceramic Society, San Francisco, October 1988.

1 Introduction

Surface structures and surface properties can affect the operating performance of a range of ceramic materials: from bulk, sintered compacts to thin ceramic films. Considerations which are particularly important to the ceramist are: a) surface diffusion, mass transport and the sintering process, b) catalysis, c) bonding and adhesion, d) corrosion and chemical reactions at surfaces, e) crystal growth and evaporation, f) interface structures and epitaxy, g) crystallographic anisotropy of surface properties, h) thermal grooving, etc. Although the need for monitoring surface structures and other surface phenomena is recognized, information recorded from ceramic surfaces is acknowledged to be very limited [1]. A large fraction of the surface data now available to the ceramist has been recorded from structures that were prepared in ultra-high vacuum (UHV) and which are therefore considered intrinsic surface structures. For example, low-energy electron diffraction (LEED) studies, which are necessarily conducted on planar specimens in UHV, have reported that the ($\sqrt{31} \times \sqrt{31}$) R9° periodicity for the (0001) α -Al₂O₃ surface may be considered an intrinsic surface structure above ~1500°C [2]. However, most present-day applications of ceramics do not require that the material be processed in a UHV environment. Surface information obtained under experimental conditions which more closely resemble those encountered during typical ceramics processing treatments is particularly lacking. This latter category of ceramic surfaces would be considered "dirty" in the strict surface-science sense [3] and yet the experimental surface conditions which typically confront the ceramist certainly would not be described as "clean".

In addition to an uncertain degree of surface cleanliness, real ceramic surfaces are not simply planar terraces but, rather, are known to be stepped [4]. Steps are sites for active catalysis and are also defect sites for the nucleation of deposited overlayers. Moreover, the intersections of dislocations with surfaces are growth sites for synthetic ceramic materials. Interactions between surface defects are therefore of interest in the field of crystal growth.

Thin ceramic films can now be produced with crystalline surfaces which possess a well-defined topography. These thin-film substrates have been prepared by standard electron microscope specimen preparation techniques and have then been annealed at a temperature sufficient to remove and/or recrystallize the layer of surface damage invariably present on the as-thinned specimens. The films are ideally suited for examination in the transmission electron microscope (TEM); they are faceted on low-index crystallographic planes and can be adapted to studies of ceramic materials which require crystalline surfaces. The annealed TEM specimens also provide templates on which surface defects, such as

steps, dislocations, stacking faults and other interfaces, and the interactions of surface defects may be examined. These annealed specimens will be shown amenable to the systematic characterization of various surface phenomena that are of interest in ceramic science. It is emphasized that these experiments are performed in air or in a moderate vacuum. The surfaces described in this study are therefore closely related to those surfaces which would be encountered during the high-temperature processing characteristic of most ceramic materials.

Surface structure and surface chemistry analyses have previously been applied to the interpretation of pore and grain-boundary phenomena and hence to sintering mechanisms. For example, at the high temperatures required for sintering ceramic materials the surfaces of individual grains within a polycrystalline ceramic compact may facet on low-index, low-energy surfaces [5]. Impinging faceted surfaces could then contribute to the development of a microstructure comprised of grain boundaries with favored grain-boundary planes. In the specific case of α - Al_2O_3 , (0001) has been shown to be a favored surface-terrace and surface-facet plane [5] and is also a favored grain-boundary and grain-boundary facet plane [6]. In addition, different segregation profiles have been reported for Mg [7,8] and Ca [8,9] impurities to α - Al_2O_3 surfaces; Mg segregates readily to (0001) and (10 $\bar{1}$ 0) surfaces while Ca segregates more readily to the (10 $\bar{1}$ 0) surface than to the (0001) surface. It has been speculated [9] that this chemical segregation behavior may account for the suppression of exaggerated grain growth in sintered MgO-doped α - Al_2O_3 powders but not in sintered CaO-doped α - Al_2O_3 powders. These observations illustrate that results recorded from the surfaces of ceramics may be extended to the interpretation of phenomena at interfaces.

Knowledge of interface structure and interface chemistry is necessary for a complete understanding of the physical properties of many materials, for example the mechanical properties of ceramic composites [10]. Another important class of interfaces is metal-ceramic interfaces which are of great importance in electronic packaging [11], the joining of ceramics to metals [12] and in metal-ceramic composite materials [13]. Research has focussed on characterizing the bonding, adhesion and wetting of metals on ceramics since this knowledge is necessary to understand the joining of these materials. The structure of individual metal-ceramic interfaces can best be studied using TEM. The annealed TEM specimens described in the present study may be used as thin-film substrates for the deposition of layers or particles of metals, semiconductors or other ceramic materials and hence for the study of interfaces and chemical reactions. These substrates have crystalline surfaces (the ion-milling damage has been removed or the amorphized material recrystallized) and can therefore be used to monitor epitaxy between thin films.

Solid-state reactions [14] are an important processing step in the production of many ceramic materials, including the sintering of thin ceramic films. The interfaces associated with these reactions are typically characterized from bulk diffusion couples, from which samples for TEM examination are prepared after the reaction has been conducted. Simpson and Carter [15] have developed a 'thin-film approach' to the characterization of oxide/oxide reactions in which the TEM specimen is thinned before the reaction is conducted and specimen-preparation artifacts are thereby avoided. For example, using this approach, the earliest stages of NiAl_2O_4 formation have been monitored by exposing $\alpha\text{-Al}_2\text{O}_3$ TEM specimens to NiO vapor at 1415°C . The thin-film approach can be extended by preparing thin-film reaction couples using a chemical-vapor deposition (CVD) technique.

There are several experimental advantages and opportunities derived from depositing thin layers of crystalline material onto crystalline substrates that were previously prepared in the form of self-supporting TEM specimens. For example, experiments can be designed to examine interface structure, with the advantage that many difficulties associated with preparing dissimilar materials for TEM characterization are overcome. These experiments thus avoid many of the pitfalls associated with characterizing interfaces in the TEM and provide the opportunity to pose new questions which can be investigated with the high spatial resolution available in the TEM. Additional advantages to this approach will be addressed in detail as the experimental observations are described. It will be shown that a critical requirement for the interface studies is the use of self-supporting TEM specimens that are prepared with clean and crystalline surfaces.

This paper describes several different experimental studies which use the TEM to analyze surface phenomena. It illustrates several applications of a particular experimental approach which is suitable for characterizing many different ceramic systems. A principal goal of this research is to record surface structure information from real ceramic materials, i.e., to prepare and characterize surfaces which are composed of steps and other defects. The response of such crystalline surfaces to subsequent heat treatments can then be examined. These specimens are also shown to be suited for the deposition of metallic or ceramic overlayers. Ceramic/ceramic and metal/ceramic interfaces can, therefore, also be examined.

In the following discussion, surface phenomena will be described that are intrinsic to the annealed thin-film TEM specimens. Illustrations of the use of these films as substrates for deposited overlayers will then be discussed. It is important to emphasize that the experiments described here do not address phenomena intrinsic to UHV-cleaned and sputtered surfaces but rather were conducted in experimental conditions which more closely approximate those encountered during the processing of "real" ceramic materials.

2 Surface Preparation

Self-supporting TEM specimens were prepared from single-crystal substrates of $\alpha\text{-Al}_2\text{O}_3^*$ and thin films of $\beta\text{-SiC}^{**}$ which had been deposited onto (100) Si substrates [16]. The "bulk" materials were prepared in the usual way for TEM examination; the final step in the thinning process was ion-milling with 4keV Ar ions until a small (~ 0.1 to 0.2mm) circular perforation formed. The perforated $\alpha\text{-Al}_2\text{O}_3$ TEM specimens were annealed in air; the $\beta\text{-SiC}$ TEM specimens were annealed in a vacuum furnace[†] operated at $\sim 3 \times 10^{-5}$ torr. This process removes and/or recrystallizes the near-surface damage induced during ion-milling. The annealing temperatures were varied from 1000°C to 1400°C . High-purity $\alpha\text{-Al}_2\text{O}_3$ furnace boats were used to shield the $\alpha\text{-Al}_2\text{O}_3$ specimens from the impurities which are typically present in high temperature furnaces (e.g., Si and Ca). The boats were first cleaned by soaking in a solution of aqua regia ($\text{HCl} + \text{HNO}_3$), boiled in distilled H_2O and then pre-fired at 1400°C . The carbide samples were similarly protected within an acid-cleaned, high-purity graphite container.

Conventional TEM was performed with a JEM1200EX operated at 120keV or a Siemens 102 operated at 125keV. A carbon layer has traditionally been deposited onto TEM specimens of highly insulating materials to minimize electrostatic charging effects. However, the single-crystal specimens used in the present study could be imaged in the TEM without depositing this thin carbon layer, although it should be noted that carbon coating was necessary to image fine-grain polycrystalline $\alpha\text{-Al}_2\text{O}_3$. Focussing and objective astigmatism corrections were performed on areas of the specimen which were adjacent to those from which images were to be recorded. This alignment procedure minimized beam-specimen interactions since prolonged exposure to the electron beam can quickly promote specimen contamination and degradation [17].

An example of a TEM specimen prepared in the manner described above is shown in Fig.1, a bright-field (BF) image of an (0001) $\alpha\text{-Al}_2\text{O}_3$ specimen (annealed in air at 1400°C for 24h). This image is comprised of patches of constant intensity (shading) which correspond to terraces of (0001)-oriented material that are separated by surface steps. Steps on the (0001) $\alpha\text{-Al}_2\text{O}_3$ surface adopt $\{11\bar{2}0\}$ and $\{10\bar{1}0\}$ planes and their height has been measured to be $\sim 3.9\text{nm}$ or three unit cells in the [0001] direction [5]. (A labelling convention has been introduced in Fig.1: the step traces, not the step planes, are labelled. Ambiguities in labelling crystallographic directions will be avoided by denoting directions with arrows; traces are denoted with lines.)

After a preliminary examination in the TEM, the specimens were removed from the microscope and then subjected to one or a series of thermal and/or chemical processing

treatments. Surface defects and the interactions between surface defects could then be analyzed.

3 Movement of individual surface steps

Changes in the relative positions of surface steps on thin ceramic films can be monitored through the sequential reheating of the TEM specimens. The (0001) α -Al₂O₃ surface is composed of a relatively simple arrangement of steps [5] as is illustrated in Fig.2A which shows a BF image recorded from an (0001) α -Al₂O₃ specimen after annealing in air at 1400°C for 24h. The steps are similar to those shown in Fig.1; they lie parallel to {10 $\bar{1}$ 0} and {1 $\bar{2}$ 10} planes. Fig.2B then shows a BF image, recorded under similar microscope operating conditions, from the same region of the (0001) α -Al₂O₃ specimen but after reheating for 3h, in air, at 1200°C. The positions of some steps on this (0001) surface have changed during the reheating. These changes are summarized in Fig.2C which is a schematic diagram superimposing the step traces from both Fig.2A and Fig.2B. Step translations are particularly evident at small (~25nm) step kinks, some of which are arrowed in Fig.2. These small kinks generally form on {11 $\bar{2}$ 0}-type planes and are offsets that are associated with longer steps on {10 $\bar{1}$ 0}-type planes. By comparing Fig.2A with Fig.2B it is clear that the positions of these small kinks have changed during the heat treatment and that the specimen has not thickened significantly since the terrace shadings in each image are essentially unchanged. The small kinks moved ~40nm during the 3h heat treatment at 1200°C. This movement corresponds to ~0.22nm/min, i.e., at 1200°C the kinks move at a rate of approximately one lattice spacing per minute.

3.1 Interaction of surface steps and dislocations

In addition to surface steps, other defects may be present in the thin ceramic films. Dislocations, for example, can be produced during the routine preparation of TEM specimens and introduced during grinding and polishing [18]. The annealed TEM specimens used in this study provide a template on which to monitor interactions between surface steps and dislocations.

Dislocations are present in the BF image recorded from an (0001) α -Al₂O₃ specimen shown in Fig.3. This figure demonstrates directly that the movement of steps can be impeded by dislocations. However, the pinned steps continue to advance during high temperature processing and begin to bow out between the dislocations. It should be noted that the steps which bow out between dislocations tend to remain aligned along low-index crystallographic planes. This observation is consistent with the step translations observed in Fig.2 where step segments remained aligned to low-index planes after thermal cycling to 1200°C. One exception to this general observation lies a few degrees away from a (10 $\bar{1}$ 0)

step plane and is arrowed in Fig. 3. This configuration may be an intermediate one prior to fully aligning parallel to a $(10\bar{1}0)$ plane.

Further interactions between surface steps and dislocations are demonstrated in Fig.4 which shows a series of BF images recorded from the same region of a (0001) α - Al_2O_3 specimen. There are several dislocations in this area of the sample in Fig.4A; some examples are indicated at "A", "B" and "C". Note that the step distribution on this specimen, which was annealed in air at 1200°C for 10min, is not the simple step distribution that was recorded from specimens which had been subjected to a 24h heat treatment at 1400°C (Fig.1 through Fig.3). The dislocations in Fig.4A pin surface steps and some examples of pinned steps are present at the dislocations arrowed at "A", "B" and "C". It should be noted that the pinned steps are comprised of straight step segments that have adopted $\{11\bar{2}0\}$ or $\{10\bar{1}0\}$ -type planes on the (0001) α - Al_2O_3 surface.

Figs 4B-E were recorded from exactly the same area of the specimen as Fig.4A but after sequentially reheating for 2h, 4h, 6h and 8h at 1200°C , respectively. The positions and distribution of steps changed during the reheating. For example, the set of finely-spaced surface-step segments near the edge of the specimen and arrowed at "D" in Fig.4A has straightened into a single step in Fig.4E. This sequence of images also demonstrates the effects of reheating on step/dislocation interactions. Pinning and bowing of steps at dislocations can be followed through the sequence of micrographs for the dislocations arrowed at "A", "B" and "C" in Fig.4A.

Surface steps have also been observed to become detached from dislocations. The step which is pinned at the dislocation at the right of "A" in Fig.4A is not pinned by this dislocation in Fig.4C. Moreover, after separating from the dislocation, this step has become more closely aligned to a single well-defined crystallographic plane. The dislocation was actually "dragged" along by the step during the detachment process. Note that the two dislocations at "A" in Fig.4A have moved relative to one another in Fig.4C; the defects are side-by-side in Fig.4A and top-to-bottom in Fig.4C. Dislocation movement has previously been reported in α - Al_2O_3 TEM specimens that were heated to 1400°C [19]; it is important to note that the dislocation movement detected here was recorded after annealing at 1200°C .

A second thermally-activated phenomenon has been recorded from dislocations in the annealed thin ceramic films and is illustrated along the row of dislocations (arrowed) that has pinned steps on the (0001) α - Al_2O_3 surface in Fig.5A. Thermal etch pits have been observed to form at some dislocations during the heat treatments. An example of a thermal etch pit is shown at "P" in Fig.5A; this symmetrical hole is very reminiscent of a small pore. The 7nm pore in Fig.5A has formed at the end of the row of dislocations. Further

illustrations of similar pores observed after annealing the sample at 17.5 and 41h at 1300°C, respectively, are presented in Figs 5B and 5C. In each case, the pores are pinning surface steps which have remained faceted on low-index planes.

In Fig.5A and Fig.5B the projected edges of the pores are circular while in Fig.5C the pore edges show a pseudo-six-fold symmetry. In each of the examples in Fig.5 the pore surfaces which extend through the specimen are faceted. The thickness fringes around the edges of the pores in Fig.5A and Fig.5B are consistent with the presence of facets that are inclined to the (0001) surface and which belong to $\langle 1\bar{1}00 \rangle$ -type zone axes; e.g., $\{11\bar{2}6\}$ -type planes. The largest pore has also faceted onto surfaces that are inclined to the (0001) surface, but the thickness fringes are more closely spaced than for the pores in Figs 5A,B which suggests that the surface of the largest pore has faceted onto planes that are more steeply inclined to (0001); e.g., $\{11\bar{2}3\}$ -type planes. These observations of pore faceting thus suggest the development of a hierarchy of facet planes, $\{11\bar{2}6\} \rightarrow \{11\bar{2}3\} \rightarrow \{11\bar{2}0\}$, with the $\{11\bar{2}0\}$ surfaces being the most energetically favorable. The largest pores would be composed of the lower-energy surfaces since these defects would contain the greatest surface area.

3.2 Interaction of steps with stacking faults

There is ~20% lattice mismatch between β -SiC and Si; this mismatch is partly accommodated by the generation of $\{111\}$ stacking faults in β -SiC films that have been deposited onto (100) Si substrates [20]. Fig.6 shows a low-magnification BF image recorded from a (100) β -SiC specimen which had been annealed in vacuum at 1300°C for 12h. The steps on the (100) β -SiC surface tend to lie parallel to $\{011\}$ planes and are therefore either parallel or perpendicular to the projected widths of the stacking faults. Several steps on the (100) β -SiC surface in Fig.6 intersect the stacking faults. Small offsets are observed at the intersections between steps and stacking faults; these offsets are arrowed in Fig.6. The offsets are, however, more readily observed in weak-beam dark-field (WBDF) images since the effective extinction distance is then significantly reduced.

Fig.7A shows a BF image recorded from a (100) β -SiC sample that had been annealed in vacuum at 1300°C for 12h. WBDF images were recorded from this area with $(02\bar{2})$ and (022) reflections and are shown in Fig.7B and Fig.7C, respectively. Two surface-step/stacking-fault intersections are arrowed in Fig.7A and the offsets which occur at these intersections are most clearly resolved in the enlargements from the WBDF images that are shown in Figs 7D,E. Note that, since each step is present on only one surface, the offset will occur at one side of the stacking fault only, as indicated at the arrows in Figs 7D,E.

The step height on the (100) β -SiC surface has been estimated by measuring the offset in the WBDF images and equals $\sim 2\text{nm}$.

3.3 Thermal Grooving

Thermal etching has been observed to occur at antiphase boundaries (APBs) in β -SiC. APBs can be generated in polar materials that are grown on non-polar substrates (β -SiC films on Si, for example) if atomic steps are present on the surface of the substrate [20]. Preferential chemical etching, specifically preferential oxidation, has been reported previously at APBs in β -SiC [21]. The present observations directly illustrate thermal etching at APBs in this material.

Fig.8A shows a BF image recorded from a (100) β -SiC film that had been annealed in vacuum for 12h at 1300°C. This image shows an APB that has intersected the edge of the TEM specimen. These faceted, planar defects have been identified as APBs [22] by monitoring the difference in crystal polarity on either side of the interface with a convergent-beam electron diffraction (CBED) experiment [23]. Fig.8B shows an enlargement of this faceted APB. Faceting has been observed frequently at APBs in β -SiC thin films; the APB in Fig.8 has faceted onto (010) and (001) segments which are edge-on and (111) segments that are inclined. The crystallography of the (111) segments was confirmed by tilting the specimen to a $[1\bar{1}0]$ zone axis and noting that these segments were then parallel to the electron beam.

A deep groove which formed at the intersection between the APB and the edge of the TEM specimen has faceted on {011}-type planes (labelled in Fig.8A). Grooving has also been recorded at the intersection between APBs and the top and bottom specimen surfaces, as shown in Fig.8B where this grooving is manifest as the light-shaded (i.e., thinner) band of material to either side of the interface at "A".

It is interesting to note that thermal grooving does not occur at the stacking faults in the β -SiC films. The stacking fault labelled "B" in Fig.8A intersects the edge of the TEM specimen but shows no evidence for grooving at this surface. In addition, this stacking fault does not show the light-shaded material that would be characteristic of a thinned region.

4 Metal/ceramic interfaces

The present experimental approach introduces a method for characterizing the earliest stages of metal-ceramic epitaxy, in particular, the influence of surface defects on particle nucleation and the growth of small metal particles on ceramic substrates can be examined directly. Metal particles are deposited onto the surface of ceramic TEM specimens which have already been annealed and characterized. Illustrations of epitactic relations, the

influence of surface defects on particle nucleation, the accommodation of lattice misfit and the growth of small particles on single-crystal ceramic substrates are presented for the Cu/ α -Al₂O₃, W/ α -Al₂O₃, W/ β -SiC and ThO₂/ β -SiC systems.

Metal particles were deposited onto the annealed TEM specimens in a manner similar to that which Morrissey, et. al. [24] used to produce Mo/ α -Al₂O₃ interfaces. A schematic diagram of the deposition chamber assembly is shown in Fig.9. The perforated TEM specimens were placed above a metallic source, typically a TEM grid or a metal foil that had been prepared into a 3mm-diameter disk, and enclosed within a ceramic container (α -Al₂O₃ for α -Al₂O₃ specimens and graphite for β -SiC specimens). The container, which was used to minimize contamination from the furnace, was pressed between two tungsten disks and this entire deposition chamber assembly was then annealed in a vacuum of $\sim 3 \times 10^{-5}$ torr.

4.1 β -SiC

For (100) β -SiC, the TEM specimen was first annealed for 2h at 1000°C and then bcc tungsten (W) particles were deposited onto this annealed film by heating the assembly for 15min at 1200°C. Fig.10A is a BF image which shows dark W particles on the (100) β -SiC surface. The small particle size precludes the recording of selected-area diffraction (SAD) patterns from individual particles. However, two important crystallographic features can be seen. No surface steps are present in this image although it was recorded from the [100] zone axis which has been shown previously to provide surface step contrast. Secondly, moiré fringes lying predominantly in one direction, are present on the smaller W particles (arrowed, for example). These fringes are indicative of a special crystallographic relationship between W and β -SiC. The moiré fringe spacing, ~ 5 nm, is consistent with the alignment of the (002) planes in the W particles with the (022) planes in the β -SiC substrate. This crystallographic orientation relation is supported by the WBDF image shown in Fig.10B, recorded with an (022) β -SiC reflection from an area adjacent to that shown in Fig.10A, where both the stacking faults in the β -SiC substrate and many of the small W particles are illuminated. The W particles must therefore be aligned with respect to the β -SiC substrate.

Both the degree of epitaxy and size of metal particles deposited onto the ceramic TEM specimens can be controlled by varying the deposition temperature and/or time. For example, the W particles shown in Fig.11A were deposited onto a (100) β -SiC TEM specimen by heating for 1h at 1200°C after the TEM specimen had been annealed at 1000°C. Well-defined step traces are present on this β -SiC surface. The presence of these step traces suggests that the ion-milling damage on the β -SiC surface in Fig.11A may have been more fully removed than was the case in Fig.10A. In addition, the W particles, which range in size from 20-50nm after heating for 1h at 1200°C, are clearly larger than those in

Fig.10A. SAD patterns could be recorded from the larger W particles and an example is shown in Fig.11B together with a schematic diagram (Fig.11C). The orientation relation between W and β -SiC is $(011)_W \parallel (020)_{\beta\text{-SiC}}$ and $(002)_W \parallel (022)_{\beta\text{-SiC}}$ with $[100]_W \parallel [100]_{\beta\text{-SiC}}$. Many W particles show moiré fringe contrast in orthogonal directions since there is nearly complete epitaxial alignment between the $(100)_W$ plane and the $(100)_{\beta\text{-SiC}}$ plane. The moiré contrast observed within each particle in Fig.10B is generated from the 2.7% lattice misfit between W and β -SiC or from small rotations about the common $[100]$ direction.

Step traces on the (100) β -SiC surface appear as both straight and curved lines in Fig.11A. Surface steps on (100) β -SiC generally adopt low-index $\{011\}$ -type planes but can become curved when pinned by barriers such as W particles. Straight step-traces along $[011]$ and $[0\bar{1}1]$ are indicated at "A" and a curved step trace is arrowed at "B". The curved steps may indicate that the 1h-heat treatment at 1200°C is not sufficient to allow all the steps to align along low-index planes. Steps on the (100) β -SiC surface have been seen to move when subjected to heat treatments, as described for α - Al_2O_3 .

4.2 α - Al_2O_3

Tungsten particles have been deposited onto the (0001) surface of α - Al_2O_3 by the approach described in §4.1, heating the assembly for 24 h at 1300°C . A BF image of such particles (arrowed) is shown in Fig.12. The particles are small, $\sim 5\text{nm}$ in diameter, and are directly attached to, or associated with, the steps on the (0001) α - Al_2O_3 surface. Dislocations are also present in Fig.12, for example at "A" and "B", and both the dislocations and the W particles pin steps on the (0001) α - Al_2O_3 surface. The steps, however, continue to adopt low-index crystallographic planes even when pinned.

Fig.13A shows a low-magnification BF image of several Cu particles deposited onto the (0001) surface of α - Al_2O_3 by heating at 700°C for 15min. This TEM specimen had been annealed previously at 1300°C for 17.5h to allow for the formation of well-defined surface steps. Most of the Cu particles are associated with surface steps. For example, Fig.13B, which has the same orientation as Fig.13A, shows a BF image recorded from four Cu particles on an (0001) α - Al_2O_3 surface. Each particle is associated with the step lying parallel to the $(1, \bar{2}, 0)$ plane.

Fig.13A also illustrates the spatial distribution of Cu particles deposited at this relatively low temperature. This low particle density allows for the examination of individual Cu particles on the (0001) α - Al_2O_3 surface. SAD patterns have been used to identify the particles as Cu metal. SAD analysis has also been used to examine the epitaxy between single Cu particles and the (0001) α - Al_2O_3 surface. Two different faceted Cu particles are shown in Fig.14A and Fig.15A. In both BF images the $\{110\}$ Cu facets are parallel to step

traces in the underlying α -Al₂O₃. The orientation relations between the particles and the (0001) substrate are illustrated in the corresponding SAD patterns (Fig.14B and Fig.15B) and schematic diagrams (Fig.14C and Fig.15C). Both Cu particles are oriented with a close-packed (111) Cu plane parallel to the pseudo-close-packed (0001) α -Al₂O₃ plane. However, the particle in Fig.14A is oriented with the {110} Cu planes nearly parallel to the {10 $\bar{1}$ 0} α -Al₂O₃ planes while the particle in Fig.15A is oriented with the {110} Cu planes rotated 30° and nearly parallel to the {11 $\bar{2}$ 0} α -Al₂O₃ planes. The Cu reflections were distinguished from the nearby double-diffraction reflections by tilting the specimen until only the Cu reflections remained. Cu particles have also been evaporated onto (11 $\bar{2}$ 0) α -Al₂O₃ specimens. Fig.16A is a BF image recorded from Cu particles that were deposited onto (11 $\bar{2}$ 0) α -Al₂O₃ at 800°C for 8h. The TEM specimen had been annealed previously for 24h at 1300°C. The orientation relation recorded from these particles was (002)_{Cu} || (0006)_{Al₂O₃} and ($\bar{2}$ 20)_{Cu} || (30 $\bar{3}$ 0)_{Al₂O₃} with [110]_{Cu} || [11 $\bar{2}$ 0]_{Al₂O₃} and is shown in the corresponding SAD pattern and schematic diagram (Fig.16B,C).

5 Ceramic/Ceramic Interfaces

Ceramic particles may also be deposited onto this type of thin ceramic substrates. For example, a ThO₂-doped W source was used for one deposition experiment. Small quantities of ThO₂ are commonly added to the W filaments used in the electric-light industry, to act as a grain-growth inhibitor [25]. ThO₂ particles were thus deposited onto a (100) β -SiC TEM specimen during the deposition of W.

Fig.17A shows a 0.5 μ m-size ThO₂ particle which was deposited onto (100) β -SiC during a 1h, 1200°C anneal. The ThO₂ particle was identified from the corresponding SAD pattern that is shown in Fig.17B together with a schematic diagram (Fig.17C, where the ThO₂ reflections are represented by small dots). The orientation relation between these phases is (022)_{ThO₂} || (002) _{β -SiC} with [100]_{ThO₂} || [100] _{β -SiC} and there is a 9.3% lattice mismatch, as measured in Fig.17B, associated with this epitactic ThO₂/ β -SiC interface. Orthogonal sets of parallel moiré fringes, with a 2.16nm spacing, are present in Fig.17 and are consistent with this mismatch between ThO₂ and β -SiC. An enlargement of these moiré fringes is inset within Fig.17A.

Superimposed on the moiré contrast in Fig.17A is a faint, broad figure with four-fold symmetry. This symmetric intensity distribution is more clearly observed from larger ThO₂ particles, such as the 1 μ m-size particle in Fig.18. The intensity distribution within this ThO₂ particle possesses four-fold symmetry and subsequent dark-field imaging and diffraction experiments showed that this ThO₂ particle had bent into a dome with the ThO₂ particle in compression. The ThO₂ reflections in Fig.17B are outside of the β -SiC

reflections and corresponds to the β -SiC having the larger lattice parameter. The dome formation is therefore not due to unrelieved strain from the misfit, but is presumably associated with a differential thermal expansion. Moiré fringes in the large ThO_2 particle are shown in the inset to Fig.18. The bend contours in the underlying β -SiC, which extend in the $\langle 010 \rangle$ β -SiC directions, demonstrate that the strain is partly accommodated by deformation of both the thin β -SiC substrate and the ThO_2 particle. The smaller ThO_2 particle in Fig.17A did not bend as severely nor did the accumulated misfit grossly deform the underlying substrate, since bend contours were not observed to extend into the β -SiC, although the onset of bend-contour formation was observed in the particle.

6 Thin-film reaction couples

NiO particles can be directly deposited onto annealed α - Al_2O_3 TEM specimens. By maintaining the deposition temperature below the NiAl_2O_4 (spinel) formation temperature, the orientation relationship between the NiO and the α - Al_2O_3 can be studied. The initial stages of NiAl_2O_4 formation and growth can then be examined by annealing the thin-film reaction couples and characterizing the sample in the TEM. Defects, such as stacking faults, are generated during the phase transformation to NiAl_2O_4 , and these defects can be monitored in the TEM. Most importantly, specific interfaces may be examined during a sequence of heat treatments; thin-film reaction kinetics can thus be studied simultaneously for different interface structures.

The NiO particles are deposited onto the annealed substrates by CVD [26]. The reactants, NiCl_2 and H_2O , are supplied by flowing an Ar carrier gas over a NiCl_2 source at $\sim 800^\circ\text{C}$ and by bubbling Ar through H_2O at 20°C . This process produces NiO particles, which formed on the surface of the α - Al_2O_3 substrate, and HCl gas. The size of the NiO particles can be adjusted by varying parameters such as the substrate temperature and the deposition time.

Fig.19 shows schematic diagrams of a typical thin-film reaction couple in which a NiO particle has been deposited onto the stepped surface of an α - Al_2O_3 TEM specimen A.) in cross-section and B.) in plan view where the step traces are shown to separate regions of uniform intensity and therefore constant thickness. The samples are then placed in an α - Al_2O_3 chamber to minimize contamination from the furnace, annealed in air and re-examined in the electron microscope. NiAl_2O_4 forms during this annealing treatment as illustrated by Fig.19C and Fig.19D which show the formation of spinel in the thin-film TEM reaction couple. The α - Al_2O_3 chamber is shown schematically in Fig.20 where the TEM specimen is protected by two single-crystal α - Al_2O_3 plates which are surrounded by α - Al_2O_3 powder and enclosed by two α - Al_2O_3 furnace boats.

The deposition of NiO particles onto the (0001) α -Al₂O₃ surface results in the formation of different orientation relationships and particle morphologies. For example, Fig.21A is a bright-field (BF) image recorded from a 400nm-wide NiO particle which was deposited onto an annealed (0001) α -Al₂O₃ TEM specimen for 3min at 860°C. The sample geometry of the thin-film reaction couple in Fig.21A is analogous to the schematic illustration shown in Fig.19B, i.e., a dark NiO particle is in contact with a faceted or stepped α -Al₂O₃ surface.

Fig.21B shows exactly the same NiO particle as that shown in Fig.21A but after a 1h anneal at 1120°C during which a layer of NiAl₂O₄ formed. It has been demonstrated that the steps on the α -Al₂O₃ surface do not propagate appreciably during short anneals at 1200°C and thus provide suitable features from which to measure the growth of the NiAl₂O₄ layer. The same surface-step trace is arrowed in both Figs 21A and 21B for reference. SAD patterns from this thin-film reaction couple showed that there was a single orientation relation between the NiAl₂O₄ layer and the α -Al₂O₃ substrate such that $(220)_{\text{NiAl}_2\text{O}_4} \parallel (11\bar{2}0)_{\alpha\text{-Al}_2\text{O}_3}$ with $[111]_{\text{NiAl}_2\text{O}_4} \parallel [0001]_{\alpha\text{-Al}_2\text{O}_3}$. In addition, the NiAl₂O₄ layer in Fig.21B has grown preferentially in the $\langle \bar{1}12 \rangle_{\text{NiAl}_2\text{O}_4}$ (i.e., $\parallel \langle 1\bar{1}00 \rangle_{\alpha\text{-Al}_2\text{O}_3}$) directions. The TEM specimen can then be subjected to further heat treatments during which the growth of NiAl₂O₄ can be further monitored. Fig.21C,D thus show the same NiO/ α -Al₂O₃ reaction couple after C.) 1h at 1200°C and D.) 2h at 1200°C. The same step trace is again arrowed in Fig.21C,D.

The defects associated with the phase transformation and solid-state reaction can also be examined in TEM. Fig.22 shows a NiO particle on an (0001) α -Al₂O₃ surface in the as-deposited state and after annealing for 1h at 1200°C during which a layer of NiAl₂O₄ formed. Fig.22C is a dark-field (DF) image recorded, after the annealing treatment, using a $\{220\}$ NiAl₂O₄ reflection. Fig.22C clearly shows stacking faults and other defects within the NiAl₂O₄ layer which link the dark NiO core to the surrounding α -Al₂O₃ matrix. It has long been established [27] that, in bulk samples, NiAl₂O₄ formation occurs at both the NiO/NiAl₂O₄ and NiAl₂O₄/ α -Al₂O₃ interfaces by the counter-diffusion of cations through the NiAl₂O₄ layer. The defects seen in Fig.22C frequently provide high-diffusivity paths through which the reaction may be accelerated [c.f., 28].

A similar reaction can be performed in which the reaction couples are intentionally exposed to furnace impurities by not enclosing the TEM specimen within the α -Al₂O₃ reaction chamber (Fig.20). A BF image from such a sample, annealed in air for 2h at 1080°C, is shown in Fig.23A. The specimen has been contaminated with Si and Ca impurities present in the high-temperature furnace. A layer of light-shaded material surrounds the faceted NiAl₂O₄ particles in Fig.23A. An energy-dispersive X-ray spectrum

(Fig.23B) was recorded from this layer to show that it is rich in Si and Ca impurities. In addition to local changes in chemistry, this siliceous material can also effect the orientation relationship between the NiAl_2O_4 and the $\alpha\text{-Al}_2\text{O}_3$. For example, two particles in Fig.23A (labelled "A" and "B") share the same surface normal but are rotated with respect to each other. SAD analysis showed that particles "A" and "B" were oriented with a $[110]$ surface normal. It is interesting to note that $\{111\}$ -type facets have developed on the NiAl_2O_4 particles that were in contact with the siliceous phase. The impurity layer isolates the NiAl_2O_4 from the $\alpha\text{-Al}_2\text{O}_3$ and hence eliminates the possibility of epitaxy between the two materials. These impurities can be minimized by conducting the reaction in a clean environment. For example, the energy-dispersive X-ray spectrum in Fig.24 was recorded from a clean NiAl_2O_4 layer and shows no evidence for Si or Ca contamination.

Single-crystal starting materials were used in the present reaction-couple experiment and hence special orientation relations may be anticipated to form at both the $\text{NiO}/\text{NiAl}_2\text{O}_4$ and $\text{NiAl}_2\text{O}_4/\alpha\text{-Al}_2\text{O}_3$ interfaces. The deposition indeed produces a range of orientation relations and some representative examples are illustrated in the SAD patterns shown in Figs.25 A.) $\{100\}_{\text{NiO}} \parallel \{100\}_{\text{NiAl}_2\text{O}_4}$, B.) $(440)_{\text{NiAl}_2\text{O}_4} \parallel (30\bar{3}0)_{\alpha\text{-Al}_2\text{O}_3}$ with $[111]_{\text{NiAl}_2\text{O}_4} \parallel [0001]_{\alpha\text{-Al}_2\text{O}_3}$ and C.) $(220)_{\text{NiAl}_2\text{O}_4} \parallel (11\bar{2}0)_{\alpha\text{-Al}_2\text{O}_3}$ with $[111]_{\text{NiAl}_2\text{O}_4} \parallel [0001]_{\alpha\text{-Al}_2\text{O}_3}$. This latter relation accurately describes that recorded from the thin-film reaction couple shown in Fig.21.

The shape of the NiAl_2O_4 reacted layer reflects its crystallography and orientation relations. The importance of the crystallographic registry between NiAl_2O_4 and $\alpha\text{-Al}_2\text{O}_3$ is supported in Fig.26 where a fully-reacted NiO particle has developed facets which are parallel to steps on the underlying (0001) $\alpha\text{-Al}_2\text{O}_3$ surface. One set of steps on the $\alpha\text{-Al}_2\text{O}_3$ surface (arrowed) has adopted $(11\bar{2}0)$ planes while the NiAl_2O_4 facet is parallel to the (220) plane.

A layer of NiAl_2O_4 with a single crystallographic orientation typically forms during the solid-state reaction between single-crystal NiO particles and (0001) $\alpha\text{-Al}_2\text{O}_3$, as was shown in Fig.21 and Fig.22. However, there are instances where the layer of NiAl_2O_4 is actually composed of two or more NiAl_2O_4 grains. Fig.27A shows a BF image recorded from two connected NiO particles on the edge of an (0001) $\alpha\text{-Al}_2\text{O}_3$ TEM specimen after a 3h heat treatment at 1200°C . SAD was used to determine that one particle was oriented with $[100]_{\text{NiO}}$ nearly parallel to the $[0001]_{\alpha\text{-Al}_2\text{O}_3}$ specimen normal; the second with $[112]_{\text{NiO}}$ nearly parallel to $[0001]_{\alpha\text{-Al}_2\text{O}_3}$. A region of NiAl_2O_4 has formed between the NiO particles and the $\alpha\text{-Al}_2\text{O}_3$ substrate. This region of NiAl_2O_4 is composed of four grains that are outlined in the schematic diagram of this reaction couple which is shown in Fig.27B. This NiAl_2O_4 region differs from the layers which have previously been

described since three distinct orientation relationships were recorded within this region. For example, a grain of NiAl_2O_4 was observed around each NiO particle and shared the cube-cube orientation relation. The first two relationships were thus recorded in Figs 27C,D ($(220)_{\text{NiAl}_2\text{O}_4}$ CDF images) where the diffracting grains of NiAl_2O_4 were aligned to the NiO particles ($\{100\}_{\text{NiO}} \parallel \{100\}_{\text{NiAl}_2\text{O}_4}$) and hence to the $\alpha\text{-Al}_2\text{O}_3$. The third relationship was recorded in Figs 27E,F ($(202)_{\text{NiAl}_2\text{O}_4}$ CDF images) where the diffracting grains, which were not in contact with the NiO, were aligned to the $\alpha\text{-Al}_2\text{O}_3$ substrate ($(111)_{\text{NiAl}_2\text{O}_4} \parallel (0001)_{\alpha\text{-Al}_2\text{O}_3}$) but do not share the cube-cube orientation relationship to the NiO.

7 Discussion

As shown above, thin ceramic films can be used to examine a range of surface phenomena in the TEM using specimens which have been subjected to annealing treatments that resulted in the formation of surface steps and other defects. The surfaces were prepared in air or in a moderate vacuum. A range of phenomena common to the surfaces of crystalline ceramic materials has been studied using this type of sample in conditions similar to those encountered during the processing of these materials. Since single-crystal specimens have been used throughout this experiment, crystallographic details have also been recorded.

7.1 Intrinsic surface phenomena

The motivation for processing ceramic materials at ever-lower temperatures is that ceramic components which are manufactured at lower temperatures are also generally produced at lower costs. For example, chemical approaches to ceramics processing, such as sol-gel technology [29,30] and the sintering of monodispersed ceramic particles [31] are partly motivated by the possibility of sintering polycrystalline ceramics to near-theoretical density at temperatures lower than those required for the processing of conventionally prepared powders. At these low temperatures, surface diffusion is an important mechanism for mass transport. Surface steps may contribute to and even dominate surface diffusion processes [4]. In addition, surface diffusion can be an important mechanism for the initial-stage sintering of ceramic powders. For the specific case of $\alpha\text{-Al}_2\text{O}_3$, initial-stage sintering has been shown to occur, in the temperature range 1100° to 1400°C , by surface redistribution [32]. The 1200° - 1400°C temperature range was used in the present study for monitoring surface step movement and it was shown that surface redistribution proceeds by mass transport along low-index crystallographic planes.

Topography, step structure and step movement on ceramic surfaces can therefore be investigated in the TEM. Step movement can be monitored by examining an annealed TEM

specimen before and after a reannealing experiment. The (0001) surface of α - Al_2O_3 was chosen for the step movement study since the distribution of steps and kinks which form on this surface, is particularly simple, being parallel to $\{11\bar{2}0\}$ and $\{10\bar{1}0\}$ planes. These steps and kinks remain straight after reheating the TEM sample. It is interesting to note that the relaxed surface energy calculated for $(11\bar{2}0)_{\alpha\text{-Al}_2\text{O}_3}$, $2.65 \text{ J}\cdot\text{m}^{-2}$, is smaller than the relaxed surface energy calculated for $(10\bar{1}0)_{\alpha\text{-Al}_2\text{O}_3}$, $2.89 \text{ J}\cdot\text{m}^{-2}$ [33]. The step movements described in this study occur through the detachment of material from step planes and its redeposition onto other nearby step planes. It might therefore be anticipated that the movement of $(11\bar{2}0)$ surfaces would be preferred [34] since the total surface energy would decrease if $(11\bar{2}0)$ surfaces were created at a faster rate than $(10\bar{1}0)$ surfaces.

Barriers to step movement, for example in the form of dislocations present in the TEM specimen, allow step interactions with other defects to be monitored. Steps that bow out between dislocations have been observed to become straight and facet along low-index planes. The steps have therefore moved in a manner consistent with the step movement recorded from the (0001) surface in Fig.2. Surface-step/dislocation interactions are encountered during crystal growth studies of synthetic materials. For example, Watanabe and Sunagawa [35] used a visible-light microscope to monitor growth pyramids on the surfaces of α - Al_2O_3 crystals that were grown from a cryolite flux. In that study growth layers were envisioned to nucleate at screw dislocation sites on the α - Al_2O_3 surface. SEM analysis showed that growth ledges on the (0001) surface, which could be resolved by reflected visible-light microscopy and may therefore be hundreds of nanometers high, possessed three-fold symmetry which strongly suggests that the growth ledges were faceted on $\{10\bar{1}0\}$ and/or $\{11\bar{2}0\}$ planes.

Other observations of barriers to step movement on the (0001) α - Al_2O_3 surface included faceted "pores". The pores form as thermal etch pits at dislocations and can pin surface steps. It is interesting to note that Dragsdorf and Webb [36] observed small ($\sim 200 \text{ nm}$ diameter) holes along the length of c -axis α - Al_2O_3 whiskers. It was shown that the holes were associated with screw dislocations whose Burgers vector was in the [0001] direction. The diameter of these "hollow-core" dislocations was consistent with the $\sim 5 \text{ nm}$ Burgers vector reported in Ref. 36 when compared to the formula that had been proposed by Frank [37].

In the present study there is evidence for the formation of holes in (0001) α - Al_2O_3 TEM specimens at sites where groups of dislocations have accumulated. It is assumed that material may be removed from regions which are strained, i.e., at dislocations, by a mechanism that is analogous to thermal etching. Fig.28 is a BF image which shows a cluster of dislocations positioned around a small area of light-shaded (i.e., thinned)

material. It is therefore proposed that clusters of dislocations may form holes which are, in principle, analogous to the hollow-core dislocations that have been recorded from c-axis α -Al₂O₃ whiskers.

The pore surfaces in the (0001) material adopted facet planes that were inclined to the (0001) surface rather than $\{11\bar{2}0\}$ or $\{10\bar{1}0\}$ facet planes. These inclined planes intersected the (0001) surface along $\langle 10\bar{1}0 \rangle$ zone axes and were therefore indexed as planes of the form $\{11\bar{2}l\}$, where $l > 0$. The preference for pore faceting on $\{11\bar{2}l\}$ planes differs from the observation of $\{11\bar{2}0\}$ and $\{10\bar{1}0\}$ step planes which form on the (0001) surface, although $\{11\bar{2}3\}$ is also a low-index plane with an associated low surface energy. It was noted, however, that large pores, i.e., those with greater pore surface area, tend to adopt facet planes that are more steeply inclined to the (0001) surface. Thus, it is suggested that a hierarchy of $\{11\bar{2}l\}$ pore facet planes exists and that the value of l decreases (and tends to zero, i.e., $\{11\bar{2}0\}$) as the pore size increases.

In addition to line defects in these samples, planar defects may be present. The intersection between planar defects and free surfaces has been monitored after a thermal cycling sequence. For example, stacking faults and APBs were recorded in thin β -SiC films and these planar defects provided an illustration of the thermal grooving phenomenon. It is noted that faceted thermal grooves are generated at the intersections between APBs and the specimen surface while no grooves are detected from intersections between stacking faults and the same surface. This observation may be consistent with the interfacial energy associated with the APB, although this quantity has not yet been measured. The interfacial energy of APBs must include contributions due to the energy associated with antisite bonding (Si-Si or C-C bonds, rather than Si-C bonds) across the interface [22]. The thermal groove may also be associated with interface stoichiometry. The APB on (100), as shown in Fig.8, is not a stoichiometric interface. The Si-C bonding is preserved across stacking faults in β -SiC and this defect may therefore possess a lower interfacial energy compared to the APB. This experiment is also suitable for the examination of thermal grooving at grain boundaries in bicrystals [38].

7.2 Interface Studies

7.2.1 Surface Preparation and Epitaxy

Orientation relationships between thick metal films and ceramic substrates have been established by cross-section TEM, as was recently demonstrated for Nb/ α -Al₂O₃ interfaces [39]. However, the cross-section technique is hampered by differential ion-thinning rates between metal films and ceramic substrates; the metal may be completely removed before the ceramic is thinned to electron transparency. Differential ion-thinning was recognized to

be the main problem in studying the Cu/ α -Al₂O₃/AlN interface [40] using the cross-section technique. In the present approach, interfaces are prepared after the TEM specimen has been thinned to electron transparency. Many of the problems and shortcomings associated with preparing interfaces of dissimilar materials for examination in the TEM are thus avoided. For example, Cu particles can be deposited directly onto thinned α -Al₂O₃ substrates. Since further thinning was not required the ion-milling problems attributable to metal/ceramic interfaces is avoided and the epitaxy between Cu and α -Al₂O₃ can be analyzed.

An ordered, crystalline substrate surface is generally required for an analysis of thin-film epitaxy between crystalline materials. Conventionally-prepared TEM specimens do not fulfill this requirement, however the annealed specimens described above do possess crystalline surfaces. Thus TEM specimens can be used as thin-film substrates for the deposition of overlayers and the initial stages of epitaxy and bonding can thus be studied.

Special surface conditions have been established for the use of TEM specimens as substrates. These surface conditions are noted, for example, in the case of W particles on (100) β -SiC where epitaxy is correlated to the surface treatment of the TEM specimen. An improvement in W/ β -SiC epitaxy, which is demonstrated in the form of an orthogonal set of parallel moiré fringes (Fig.11A), is recorded from surfaces which have been subjected to an annealing treatment that is sufficient to produce surface steps (1200°C, 1h); poorer W/ β -SiC epitaxy is noted on β -SiC surfaces that are annealed for a shorter time (1200°C, 15min) and where surface steps are not observed. It is therefore necessary to provide thin-film substrates (TEM specimen) that have crystalline surfaces and it has been shown that such surfaces can be prepared by annealing the thin oxide films in air or in a moderate vacuum.

In addition to a crystalline surface structure, the surface must also be clean. It is observed that when NiO/ α -Al₂O₃ reaction couples are heated in air, in the presence of Si and Ca (i.e., impurities common to many high-temperature furnaces), a layer of siliceous material forms between the NiAl₂O₄ reaction product and the α -Al₂O₃ substrate (TEM specimen), and NiAl₂O₄/ α -Al₂O₃ epitaxy is reduced. Thin-film reactions are thus conducted within a container manufactured from high-purity α -Al₂O₃ components to minimize contamination and to maximize direct contact between the reactants.

7.2.2 Influence of surface steps on deposited metal and ceramic particles

Small metal particles can readily nucleate at surface steps. For example, the ~5nm tungsten particles on the (0001) α -Al₂O₃ surface were attached to the ~3.9nm-high steps. These small particles had pinned the surface steps in a manner which is reminiscent of the step pinning at dislocations on the (0001) surface. Fig.12 showed that although some steps are pinned by W particles, the steps remain faceted on low-index crystallographic planes.

This faceting behavior is consistent with the step movement observations recorded from the (0001) surface (Fig.2). It will be shown below that the surface steps may also influence crystallographic characteristics of larger particles observed during the course of this interface study. Similar observations of surface steps acting as nucleation sites have been demonstrated for NaCl, for example, where visible-light microscopy has been used to examine the nucleation of Au particles [41].

Using this approach, two orientation relations have been found for Cu particles on (0001) α -Al₂O₃. The relation $\{220\}_{\text{Cu}} \parallel \{30\bar{3}0\}_{\alpha\text{-Al}_2\text{O}_3}$ is that which has been reported by X-ray diffraction experiments [42] while the relation $\{220\}_{\text{Cu}} \parallel \{22\bar{4}0\}_{\alpha\text{-Al}_2\text{O}_3}$ has not been reported previously. The observations of Katz and those discussed in the present study clearly show $(111)_{\text{Cu}} \parallel (0001)_{\alpha\text{-Al}_2\text{O}_3}$. (It had recently been concluded that the (111) planes of Cu particles do not align parallel to the (0001) plane of an α -Al₂O₃ substrate [43].)

The question which remains is: why is the latter orientation relation observed in this study? Two explanations for this observation are suggested. The first explanation for the occurrence of two orientation relationships for Cu on (0001) α -Al₂O₃, is supported by this new experimental approach to metal/ceramic interfaces, namely that surface defects may influence the epitaxy between the particles and the substrate. The shape of the Cu particles is reminiscent of cuboid-octahedra, which is the shape adopted by other small fcc-metal particles, such as Pt [44], that have been deposited onto thin ceramic films. Surface steps underlie the Cu particles shown in Fig.14 and Fig.15. In Fig.14A a $(01\bar{1})_{\text{Cu}}$ facet is parallel to a $(01\bar{1}0)_{\alpha\text{-Al}_2\text{O}_3}$ step trace (arrowed) that passes beneath the particle. In Fig.15A a $(01\bar{1})_{\text{Cu}}$ facet lies parallel to a $(11\bar{2}0)_{\alpha\text{-Al}_2\text{O}_3}$ step trace. It is therefore suggested that the surface steps may control the epitaxial relations recorded from Cu particles on the faceted (0001) α -Al₂O₃ surface. This situation would then be similar to graphoepitaxy [45] wherein crystalline particles adopt epitaxial relations that are determined by relief features, such as steps, on the surface of a substrate. Graphoepitaxy, with specific reference to Cu particles on (0001) α -Al₂O₃, is illustrated schematically in Fig.29. Note that in Fig.29A the $(110)_{\text{Cu}}$ facet is parallel to the $(1\bar{1}00)_{\alpha\text{-Al}_2\text{O}_3}$ step trace and in Fig.29B the $(110)_{\text{Cu}}$ facet is parallel to the $(11\bar{2}0)_{\alpha\text{-Al}_2\text{O}_3}$ step trace, i.e. rotated 30° with respect to Fig.29A.

However, graphoepitaxy is not the only factor which must be considered. Fig.13B showed four Cu particles which were attached to a surface step. Both Cu/(0001) α -Al₂O₃ orientation relations may be present along this $(11\bar{2}0)_{\alpha\text{-Al}_2\text{O}_3}$ step trace since particle "C" appears to be rotated 30° with respect to particles "A" and "B". A second consideration is suggested by the SAD patterns in Fig.14 and Fig.15. In Fig.14C the $\{220\}_{\text{Cu}}$ reflections are outside the $\{30\bar{3}0\}_{\alpha\text{-Al}_2\text{O}_3}$ reflections while in Fig.15C these reflections are inside the

$\{22\bar{4}0\}$ α - Al_2O_3 reflections. The lattice misfit between the Cu particle and the substrate in Fig.14 is 7.0% (tensile) and in Figs.15 the misfit is 7.4% (compressive). It is therefore suggested that the two orientation relations of Cu particles on the (0001) α - Al_2O_3 surface may form due to the similar magnitudes of the lattice misfit. A combination of graphoepitaxy and similarity in lattice misfit may also account for the two relations.

It should be noted that the orientation relationships between the Cu particles and (0001) α - Al_2O_3 are not exact but are slightly rotated about the common $[111]_{\text{Cu}} \parallel [0001]_{\alpha\text{-Al}_2\text{O}_3}$ direction. This rotation was measured as $\sim 3.5^\circ$ in Fig.14B and $\sim 1.5^\circ$ in Fig.15B, both clockwise with respect to the α - Al_2O_3 . Similar small rotations, away from exact epitaxy, have been observed for NiAl_2O_4 particles on α - Al_2O_3 [46] and for Nb films on α - Al_2O_3 [39]. These rotations presumably help to relieve the misfit strain between the Cu particles and the α - Al_2O_3 substrate rather than generate misfit dislocations.

7.2.3 Thin-Film Reaction Couples

The chemical-vapor deposition of single-crystal NiO particles onto single-crystal α -Al₂O₃ substrates has been shown to produce samples which are suited for the study of epitactic relations and solid-state reactions in the electron microscope. Each NiO particle is bonded to the α -Al₂O₃ substrate and can be used to form a microscopic reaction couple or bicrystal whose geometry is similar to the lateral diffusion couple [47]. This technique thus overcomes the bonding or joining problems which had been associated with the study of the reaction between single crystals of MgO [48] or NiO [49] and an α -Al₂O₃ single crystal. In these previous studies the rocksalt-structure oxide was not originally bonded to the α -Al₂O₃ and often became detached from the spinel layer. The CVD approach outlined in the present study can clearly produce NiO particles which are in epitactic alignment to α -Al₂O₃ and which remain in contact with the NiAl₂O₄ layer after the reaction is conducted. A further advantage of the present experimental technique is that since the NiO deposition temperature is maintained below the reaction temperature, NiO/ α -Al₂O₃ epitaxy can be monitored even though NiO and α -Al₂O₃ cannot be in contact at thermodynamic equilibrium. The NiO particles can adopt different orientations on an (0001) α -Al₂O₃ substrate and therefore solid-state reactions can be analyzed for different NiO/ α -Al₂O₃ orientation relations on the same TEM specimen. This CVD experiment thus lends itself to the examination of phase transformation kinetics as a function of interface structure.

Previous studies of bulk reaction couples have shown that the counter-diffusion of cations leads to the formation of NiAl₂O₄ during the solid-state reaction between NiO and α -Al₂O₃ [29]. In addition, studies from bulk reaction couples have shown that one NiAl₂O₄ orientation forms at the NiO/NiAl₂O₄ interface while a second orientation forms at the NiAl₂O₄/ α -Al₂O₃ interface [47,48]. Two NiAl₂O₄ orientations have also been observed in the present thin-film reaction couple experiment although a single NiAl₂O₄ orientation forms around most NiO particles.

An explanation for the formation of one or two NiAl₂O₄ orientations is presented schematically in Fig.30. A single NiAl₂O₄ orientation might be expected to form from a NiO particle which shares a special orientation relation with the α -Al₂O₃ substrate as long as this relation is also special for NiAl₂O₄. Fig.30A shows a NiO region which shares a special orientation relation to the α -Al₂O₃ region (crystallographic registry is denoted by the continuous parallel lines drawn across the NiO/ α -Al₂O₃ interface). NiO and NiAl₂O₄ are expected to share such special orientation relations since their crystal structures and oxygen sublattices are similar. A single NiAl₂O₄ orientation (I) is thus shown in Fig.30B, in crystallographic continuity, which represents Fig.30A after a heat treatment. For example, a (111)-oriented NiO particle on an (0001) α -Al₂O₃ substrate, such as those

shown in Fig.21 and Fig.22, would be expected to react and form one NiAl_2O_4 layer oriented such that $(111)_{\text{NiO}} \parallel (111)_{\text{NiAl}_2\text{O}_4} \parallel (0001)_{\alpha\text{-Al}_2\text{O}_3}$.

In contrast, two orientations of NiAl_2O_4 would be expected to form if the NiO particle were oriented to the $\alpha\text{-Al}_2\text{O}_3$ substrate in a manner which was not a special orientation for the NiAl_2O_4 . This situation is illustrated schematically in Fig.30C where no crystallographic continuity is present across the NiO/ $\alpha\text{-Al}_2\text{O}_3$ interface. One NiAl_2O_4 orientation then forms at the NiO/ NiAl_2O_4 interface (I) with the cube-cube relation while a second orientation (II) forms at the $\text{NiAl}_2\text{O}_4/\alpha\text{-Al}_2\text{O}_3$ interface (Fig.30D). This situation is reminiscent of the case of the bulk reaction couple and was clearly demonstrated with reference to Fig.27. In Fig.27 the two NiO particles did not share an orientation relation to the $\alpha\text{-Al}_2\text{O}_3$ which was as special for the NiAl_2O_4 and thus two NiAl_2O_4 orientations were observed.

8 Conclusions

A range of different surface phenomena can be studied using thinned ceramic single-crystal TEM specimens which have been annealed after thinning to electron transparency. The surfaces of these annealed specimens were crystalline and faceted. These specimens were prepared in conditions which are closely related to those present during the processing of most ceramic materials. Mass transport has been observed on the (0001) $\alpha\text{-Al}_2\text{O}_3$ surface. Small (~25nm) kinks on the steps on this surface have been monitored before and after reheating the sample at 1200°C. The steps show a strong tendency to lie along low-index crystallographic planes. Interactions between surface steps and other defects, e.g., dislocations and stacking faults, have also been analyzed. Thermal etching can also be monitored at dislocations in $\alpha\text{-Al}_2\text{O}_3$ and at APBs in $\beta\text{-SiC}$ and shown to occur along low-index planes.

The annealed TEM specimens can also be used as substrates for the deposition of other materials. Interfaces can therefore be formed after the TEM specimen has been prepared. This method can then be used to study metal-ceramic interfaces, such as $\text{Cu}/\alpha\text{-Al}_2\text{O}_3$ and $\text{W}/\beta\text{-SiC}$, and ceramic/ceramic interface, such as $\text{ThO}_2/\beta\text{-SiC}$, which are difficult to study using conventional cross-section techniques because of differential ion-thinning or where sample preparation may influence the interface structure.

The earliest stages of epitaxy can be examined using this approach as illustrated by observations on the $\text{W}/\beta\text{-SiC}$, $\text{Cu}/\alpha\text{-Al}_2\text{O}_3$ and $\text{ThO}_2/\beta\text{-SiC}$ systems. Metal and ceramic particles tend to be oriented such that low-index planes in the particles and in the single-crystal ceramic substrates were closely parallel. The lattice misfit between the particles and ceramic substrates can be accommodated by various distortions including bending of both

the thin film and the particle (ThO_2 on $\beta\text{-SiC}$) and small rotations about common crystallographic directions (Cu on $\alpha\text{-Al}_2\text{O}_3$).

Thin-film NiO/ $\alpha\text{-Al}_2\text{O}_3$ reaction couples can be prepared for TEM examination by depositing single-crystal particles of NiO onto annealed $\alpha\text{-Al}_2\text{O}_3$ TEM specimens by a low-temperature CVD process. The reaction couples can be annealed to form NiAl_2O_4 by solid-state reaction. Special crystallographic relations can then be identified and NiAl_2O_4 growth shown to depend upon the crystallographic relation between the NiO particle and the $\alpha\text{-Al}_2\text{O}_3$ substrate.

Acknowledgment

The authors would like to thank Mr Scott Summerfelt for extensive collaboration on the CVD experiments and Ms Lisa Tietz for carefully criticizing the manuscript. Mr Ray Coles has continued his careful maintenance of the electron microscopes which are a Facility supported, in part, by NSF through the Materials Science Center at Cornell. They also thank Ms M. Fabrizio for photographic work. This experimental approach using thin ceramic films was developed as part of a program supported by the US Department of Energy (grant No. DE-FGO2-89ER45381.A000). The study of phase boundaries has been supported by the US National Science Foundation (DMR-8521834). The study of metal/ceramic reactions has been supported, in part by IBM and in part by the US ARO (contract No.DAAL03-87-K-0104).

9 References

1. V.E. Henrich, "The Surfaces of Metal Oxides," Rep. Prog. Phys., **48**, 1481-1541 (1985).
2. C.C. Chang, "LEED Studies of the (0001) Face of α -Alumina," J. Appl. Phys., **39** [12] 5570-73 (1968).
3. A.M. Stoneham, "Ceramic Surfaces: Theoretical Studies," J. Am. Ceram. Soc., **64** [1] 54-60 (1981).
4. P.W. Tasker and D.M. Duffy, "The Structure and Properties of the Stepped Surfaces of MgO and NiO," Surf. Sci., **137**, 91-102 (1984).
5. D.W. Susnitzky, Y. Kouh Simpson, B. C. De Cooman and C.B. Carter, "The Structure of Surface Steps on Low-Index Planes of Oxides," Proc. Mater. Res. Soc. Symp., **60**, 219-26 (1986).

6. K.J. Morrissey and C.B. Carter, "Special Grain Boundaries in Alumina," *Proc. Mater. Res. Soc. Symp.*, **24**, 121-27 (1984).
7. S. Baik, D.E. Fowler, J.M. Blakely and R. Raj, "Segregation of Mg to the (0001) Surface of Doped Sapphire," *J. Am. Ceram. Soc.*, **68** [5] 281-86 (1985).
8. S.M. Mukhopadhyay, A.P. Jardine, J.M. Blakely and S. Baik, "Segregation of Magnesium and Calcium to the (10 $\bar{1}$ 0) Prismatic Surface of Magnesium-Implanted Sapphire," *J. Am. Ceram. Soc.*, **71** [5] 358-62 (1988).
9. S. Baik and C.L. White, "Anisotropic Calcium Segregation to the Surface of Al₂O₃," *J. Am. Ceram. Soc.*, **70** [9] 682-88 (1987).
10. F. Lin, T. Marieb, A.A. Morrone and S.R. Nutt, "Thermal Oxidation of Al₂O₃-SiC Whisker Composites: Mechanisms and Kinetics," *Proc. Mat. Res. Soc. Symp.*, **129**, in press, (1988).
11. E.A. Geiss, K.-N. Tu and D.R. Uhlmann, Eds., "Electronic Packaging Materials Science," *Proc. Mat. Res. Soc. Symp.*, **40**, (1985).
12. R.E. Loehman and A.P. Tomsia, "Joining of Ceramics," *Am. Ceram. Soc. Bull.*, **67** [2] 375-87 (1988).
13. L.S. Sigl and H.F. Fischmeister, "On the Fracture Toughness of Cemented Carbides," *Acta Metall.*, **36** [4] 887-97 (1988).
14. H. Schmalzried, *Solid State Reactions*, Verlag Chemie, Weinheim (1981).
15. Y. Kouh Simpson and C.B. Carter, "A New Approach to the Study of Solid-State Reactions," *Philos. Mag. Lett.*, **53** [1] L1-L5 (1986).
16. P. Liaw and R.F. Davis, "Epitaxial Growth and Characterization of β -SiC Thin Films," *J. Electrochem. Soc.*, **132** [3] 642-48 (1985).
17. D.J. Smith, L.A. Bursill and D.A. Jefferson, "Atomic Imaging of Oxide Surfaces I. General Features and Surface Rearrangements," *Surf. Sci.*, **175**, 673-83 (1986).
18. B.J. Hockey, "Observations by Transmission Electron Microscopy on the Subsurface Damage Produced in Aluminum Oxide by Mechanical Polishing and Grinding," *Proc. Brit. Ceram. Soc.*, **20**, 95-115 (1972).
19. T.E. Mitchell, B.J. Pletka, D.S. Phillips and A.H. Heuer, "Climb Dissociation of Dislocations in Sapphire (α -Al₂O₃)," *Philos. Mag.*, **34** [3] 441-51 (1976).
20. H.S. Kong, Y.C. Wang, J.T. Glass and R.F. Davis, "The Effect of Off-Axis Si (100) Substrates on the Defect Structure and Electrical Properties of β -SiC Thin Films," *J. Mater. Res.*, **3** [3] 521-30 (1988).

21. C.H. Carter, R.F. Davis and S.R. Nutt, "Transmission Electron Microscopy of Process-Induced Defects in β -SiC Thin Films," *J. Mater. Res.*, **1** [6] 811-19 (1987).
22. K.L. More, J. Bentley and R.F. Davis, "Antiphase Boundaries in β -SiC Thin Films," *Proc. Ann. Meet. EMSA*, **45**, 282-83 (1987).
23. J. Taftø and J.C.H. Spence, "A Simple Method for the Determination of Structure-Factor Phase Relationships and Crystal Polarity Using Electron Diffraction," *J. Appl. Cryst.*, **15**, 60-64 (1982).
24. K.J. Morrissey, K.K. Czanderna, C.B. Carter and R.P. Merrill, "Growth of α - Al_2O_3 Within a Transition Alumina Matrix," *J. Am. Ceram. Soc.*, **67** [5] C-88-C-90 (1984).
25. D. McClean, *Grain Boundaries in Metals*, Oxford University Press, Oxford, 1957.
26. R.E. Cech and E.I. Alessandrini, "Preparation of FeO, NiO and CoO Crystals by Halide Decomposition," *Trans. ASM*, **51**, 150-61 (1959).
27. E. Koch and C. Wagner, "Formation of Ag_2HgI_4 from AgI and HgI_2 by Reaction in the Solid State," *Z. Phys. Chem.*, **B34** [3-4] 317-21 (1936).
28. C.B. Carter and H. Schmalzried, "The Growth of Spinel in Al_2O_3 ", *Phil. Mag.* **A52** (2), 207-224 (1985).
29. C.J. Brinker, D.E. Clarke and D.R. Ulrich, eds., "Better Ceramics Through Chemistry," *Proc. Mat. Res. Soc. Symp.* **32**, (1984).
30. C.J. Brinker, D.E. Clarke and D.R. Ulrich, eds., "Better Ceramics Through Chemistry II," *Proc. Mat. Res. Soc. Symp.* **73**, (1986).
31. E.A. Barringer, R. Brook and H.K. Bowen, "The Sintering of Monodisperse TiO_2 ," *Mat. Sci. Res.*, **16**, 1-21 (1984).
32. J.M. Dynys, "Sintering Mechanisms and Surface Diffusion for Aluminum Oxide," Ph.D. Thesis, Massachusetts Institute of Technology, 1982.
33. P.W. Tasker, "Surfaces of Magnesia and Alumina," *Adv. Ceram.*, **10**, 176-188 (1984).
34. P. Hartman, "The Attachment Energy as a Habit Controlling Factor, III. Applications to Corundum," *J. Cryst. Growth*, **49**, 166-70 (1980).
35. K. Watanabe and I. Sunagawa, "Surface Micro-Topography of Corundum Crystals Grown From Cryolite Flux," *J. Crystal Growth*, **57**, 367-78 (1982).
36. R.D. Dragsdorf and W.W. Webb, "Detection of Screw Dislocations in α - Al_2O_3 Whiskers," *J. Appl. Phys.*, **29** [5] 817-19 (1958).

37. F.C. Frank, "Capillary Equilibria of Dislocated Crystals," *Acta. Cryst.* **4**, 497-501 (1951).
38. C.B. Carter and Y. Kouh Simpson, "Thin-Film Reactions," *Ber. Bunsenges. Phys. Chem.* **90**, 676-680 (1986).
39. K. Burger, W. Mader and M. Rühle, "Structure, Chemistry and Diffusion Bonding of Metal/Ceramic Interfaces," *Ultramicroscopy*, **22**, 1-14 (1987).
40. P. Kluge-Weiss and J. Gobrecht, "Directly Bonded Copper Metallization of AlN Substrates for Power Hybrids," *Proc. Mat. Res. Soc. Symp.*, **40**, 399 (1985).
41. G.A. Bassett, "A New Technique for Decoration of Cleavage and Slip Steps on Ionic Crystal Surfaces," *Philos. Mag., Ser. 8*(3), 1042-45 (1958).
42. G. Katz, "The Epitaxy of Copper on Sapphire," *Appl. Phys. Lett.* **12** [5] 161-63 (1968).
43. S.T. Lin and P.D. Ownby, "A Microscopic Study of Preferred Orientation and Adhesion of Solid Copper Particles on (0001) Sapphire Substrates," *J. Mater. Sci.*, **23**, 3187-94 (1988).
44. T. Wang, C. Lee and L.D. Schmidt, "Shape and Orientation of Supported Pt Particles," *Surf. Sci.*, **163**, 181-97 (1985).
45. H.I. Smith and D.C. Flanders, "Oriented Crystal Growth on Amorphous Substrates Using Artificial Surface-Relief Gratings," *Appl. Phys. Lett.*, **32** [6] 349-51 (1978).
46. C.B. Carter and Y. Kouh Simpson, "Thin-Film Reactions," *Ber. Bunsenges. Phys. Chem.*, **90**, 676-80 (1986).
47. S.H. Chen, L.R. Zheng, C.B. Carter and J.W. Mayer, "Transmission Electron Microscopy Studies on the Lateral Growth of Nickel Silicides," *J. Appl. Phys.*, **57** [2] 258-63 (1985).
48. R.C. Rossi and R.M. Fulrath, "Epitaxial Growth of Spinel by Reaction in the Solid State," *J. Am. Ceram. Soc.*, **46** [3] 145-49 (1963).
49. F.S. Pettit, E.H. Randklev and E.J. Felten, "Formation of NiAl₂O₄ by Solid-State Reaction," *J. Am. Ceram. Soc.*, **49** [4] 199-203 (1966).

* Adolf Meller Company, Providence, RI.

** Courtesy of Professor R.F. Davis, North Carolina State University, Raleigh, NC.

† Model M60, Centorr Associates, Suncook, NH.

Figure Captions

- Fig.1 (0001)- α - Al_2O_3 surface annealed for 24h in air at 1400°C. Steps lie parallel to $\{11\bar{2}0\}$ and $\{10\bar{1}0\}$ planes.
- Fig.2 Step movement on (0001) α - Al_2O_3 surface. Same area of specimen shown A.) after 24h at 1400°C and B.) after a further heat treatment at 1200°C for 3h. C.) Schematic diagram of "A" and "B" with differences, or step movement, denoted by dotted lines. Reference arrows are included for examining individual step kinks.
- Fig.3 Step pinning at dislocations on (0001) α - Al_2O_3 surface. Note that as the steps bow out, they still tend to lie parallel to low-index crystallographic planes.
- Fig.4 Steps on an (0001) α - Al_2O_3 surface interacting with dislocations during an annealing sequence at 1200°C after A.) 10min, B.) 2h, C.) 4h, D.) 6h and E.) 8h.
- Fig.5 Thermal etch pits or "pores" formed in (0001) α - Al_2O_3 surface. A.) 7nm Pore is associated with row of dislocations (arrowed). B.) 50nm circular pore faceted on planes inclined to (0001). C.) 150nm pore showing pseudo-six fold symmetry and pinning surface steps.
- Fig.6 BF image of surface step/stacking fault intersections (arrowed, for example) on (100) β -SiC.
- Fig.7 Step / stacking fault intersections on (100) β -SiC. A.) BF image and B.) (02 $\bar{2}$) and C.) (022) WBDF images. Note intersections (arrowed) and offsets (enlarged and arrowed in "D" and "E") that occur on one side of stacking fault only.
- Fig.8 Thermal groove at intersection between APB and surface of (100) β -SiC. A.) Groove faceted on $\{011\}$ planes. Note absence of groove at stacking fault labelled "B". B.) Preferential thinning or grooving recorded from top and bottom surfaces as light-shaded material at "A".
- Fig.9 Schematic diagram of metal evaporation chamber. Perforated TEM specimen placed above metal foil and enclosed within ceramic container.

- Fig.10 Tungsten particles on (100) β -SiC surface after 15min at 1200°C. A.) Moiré fringes (arrowed, for example) present in one direction in particles. Note absence of surface steps. B.) Centered-dark field image recorded with (022) β -SiC reflection both stacking faults and tungsten particles illuminated.
- Fig.11 Tungsten particles on (100) β -SiC surface after 1h at 1200°C. A.) BF image showing surface steps and tungsten particles with Moiré fringes in orthogonal directions and B.) corresponding SAD pattern and C.) schematic diagram illustrating orientation relation, $\{020\}_W \parallel \{022\}_{\beta\text{-SiC}}$ with $[100]_W \parallel [100]_{\beta\text{-SiC}}$.
- Fig.12 Small tungsten particles (arrowed) and dislocations (labelled at "A" and "B") pinning steps on (0001) α -Al₂O₃ surface.
- Fig.13 Copper particles evaporated onto (0001) α -Al₂O₃ surface and generally associated with steps on the surface. A.) Low-magnification BF image of particle distribution and B.) four copper particles aligned to step on (11 $\bar{2}$ 0) plane.
- Fig.14 Copper particle on (0001) α -Al₂O₃ surface with $\{220\}_{Cu} \parallel \{30\bar{3}0\}_{\alpha\text{-Al}_2\text{O}_3}$. A.) BF image, B.) corresponding SAD pattern and C.) schematic diagram. Note that $\{220\}_{Cu}$ reflections are outside the $\{30\bar{3}0\}_{\alpha\text{-Al}_2\text{O}_3}$ reflections.
- Fig.15 Copper particle on (0001) α -Al₂O₃ surface with $\{220\}_{Cu} \parallel \{22\bar{4}0\}_{\alpha\text{-Al}_2\text{O}_3}$. A.) BF image, B.) corresponding SAD pattern and C.) schematic diagram. Note that $\{220\}_{Cu}$ reflections are inside the $\{22\bar{4}0\}_{\alpha\text{-Al}_2\text{O}_3}$ reflections.
- Fig.16 A.) Low-magnification BF image of copper particles on (11 $\bar{2}$ 0) α -Al₂O₃ surface, B.) SAD pattern and C.) schematic diagram of orientation relation, $(002)_{Cu} \parallel (0006)_{Al_2O_3}$ and $(2\bar{2}0)_{Cu} \parallel (3\bar{3}00)_{Al_2O_3}$ with $[110]_{Cu} \parallel [11\bar{2}0]_{Al_2O_3}$.
- Fig.17 ThO₂ particle on (100) β -SiC surface. A.) BF image, B.) corresponding SAD pattern and C.) schematic diagram which shows $(002)_{\beta\text{-SiC}} \parallel (022)_{ThO_2}$ with $[100]_{\beta\text{-SiC}} \parallel [100]_{ThO_2}$. Moiré fringe periodicity in "A" (2.16nm) consistent with 9.3% lattice misfit.

- Fig.18 1 μ m-size ThO₂ particle on (100) β -SiC showing four-fold bend contour pattern in ThO₂ particle and bending in substrate in $\langle 010 \rangle$ directions.
- Fig.19 Schematic illustration of thin-film reaction couple with NiO particle deposited onto faceted surface of annealed α -Al₂O₃ TEM specimen A.) in cross section and B.) in plan view. NiAl₂O₄ layer forms during subsequent annealing and is shown in "C" and "D".
- Fig.20 Schematic illustration of assembly used for annealing thin-film reaction couple. TEM specimen is placed in single-crystal α -Al₂O₃ container, surrounded by high-purity α -Al₂O₃ powder and enclosed within α -Al₂O₃ furnace boats.
- Fig.21 BF images of NiO particle on (0001) α -Al₂O₃ surface. A.) As deposited and after B.) 1h at 1120°C, C.) 1h at 1200°C and D.) 2h at 1200°C during which NiAl₂O₄ layer formed. Arrows indicate same step trace in each image.
- Fig.22 BF images of NiO particle on (0001) α -Al₂O₃ surface A.) as deposited and B.) after 1h at 1200°C during which NiAl₂O₄ layer formed. C.) (220)_{NiAl₂O₄} CDF image showing stacking faults and other defects within NiAl₂O₄ layer.
- Fig.23 Contaminated thin-film reaction couple. A.) BF image showing light-shaded siliceous layer between NiAl₂O₄ particles and α -Al₂O₃ substrate, B.) EDS spectrum recorded from contamination layer showing presence of Si and Ca impurities.
- Fig.24 EDS spectrum from NiAl₂O₄ layer not contaminated with furnace impurities.
- Fig.25 SAD patterns recorded from interfaces with special orientation relations. A.) {100}_{NiO} \parallel {100}_{NiAl₂O₄}, B.) (440)_{NiAl₂O₄} \parallel (30 $\bar{3}$ 0)_{Al₂O₃} with [111]_{NiAl₂O₄} \parallel [0001]_{Al₂O₃} and C.) (220)_{NiAl₂O₄} \parallel (11 $\bar{2}$ 0)_{Al₂O₃} with [111]_{NiAl₂O₄} \parallel [0001]_{Al₂O₃}.
- Fig.26 BF image from fully reacted NiO particle which developed facets parallel to step traces on α -Al₂O₃ surface.

Fig.27 A.) BF image of NiO particles reacted with (0001) α -Al₂O₃ for 3h at 1200°C and B.) corresponding schematic diagram with domains of NiAl₂O₄ outlined. C,D.) (220)_{NiAl₂O₄} CDF images recorded from NiAl₂O₄ domains in contact with NiO. E,F.) (202)_{NiAl₂O₄} CDF images recorded from NiAl₂O₄ domains in contact with α -Al₂O₃ only.

Fig.28 BF image of dislocation cluster circling thinned area on (0001) α -Al₂O₃ surface.

Fig.29 Schematic illustration of graphoepitaxy between faceted Cu particles and faceted (0001) α -Al₂O₃ surface. A.) (110)_{Cu} facet parallel to (1 $\bar{1}$ 00) _{α -Al₂O₃} step trace and B.) (110)_{Cu} facet parallel to (11 $\bar{2}$ 0) _{α -Al₂O₃} step trace.

Fig.30 Schematic illustrations of possible reaction-couple geometries. A.) NiO is oriented to α -Al₂O₃ (denoted by continuous lines across NiO/ α -Al₂O₃ interface) from which B.) one layer of NiAl₂O₄ forms. C.) NiO not oriented to α -Al₂O₃ (discontinuity at NiO/ α -Al₂O₃ interface) and D.) two layers of NiAl₂O₄ form, I in registry with NiO and II in registry with α -Al₂O₃.

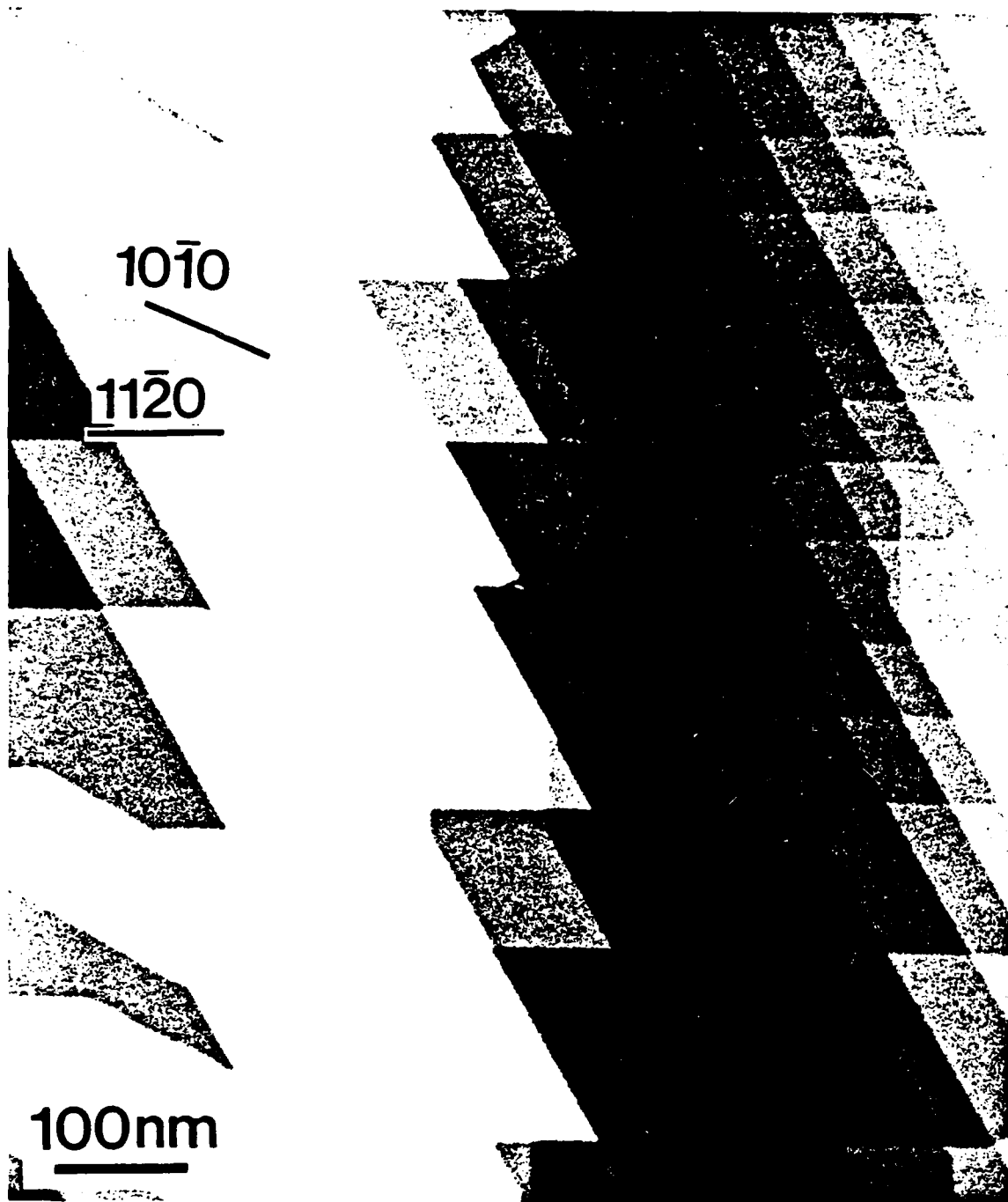


Fig.1 (0001) -Al₂O₃ surface after 24h in air at 1400°C. Steps adopt {1120} and {1010} step planes.

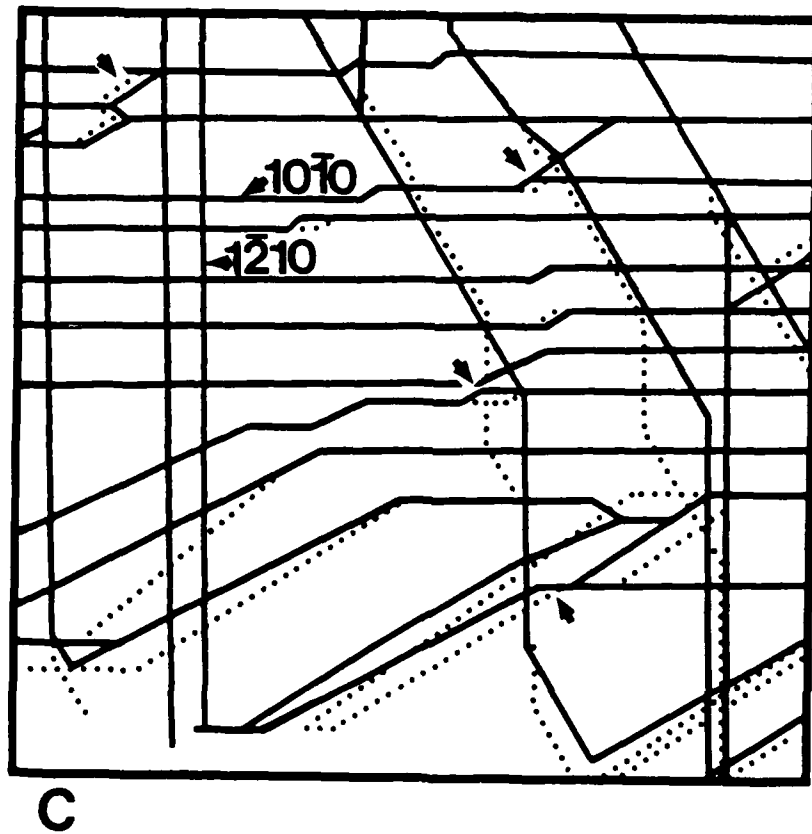
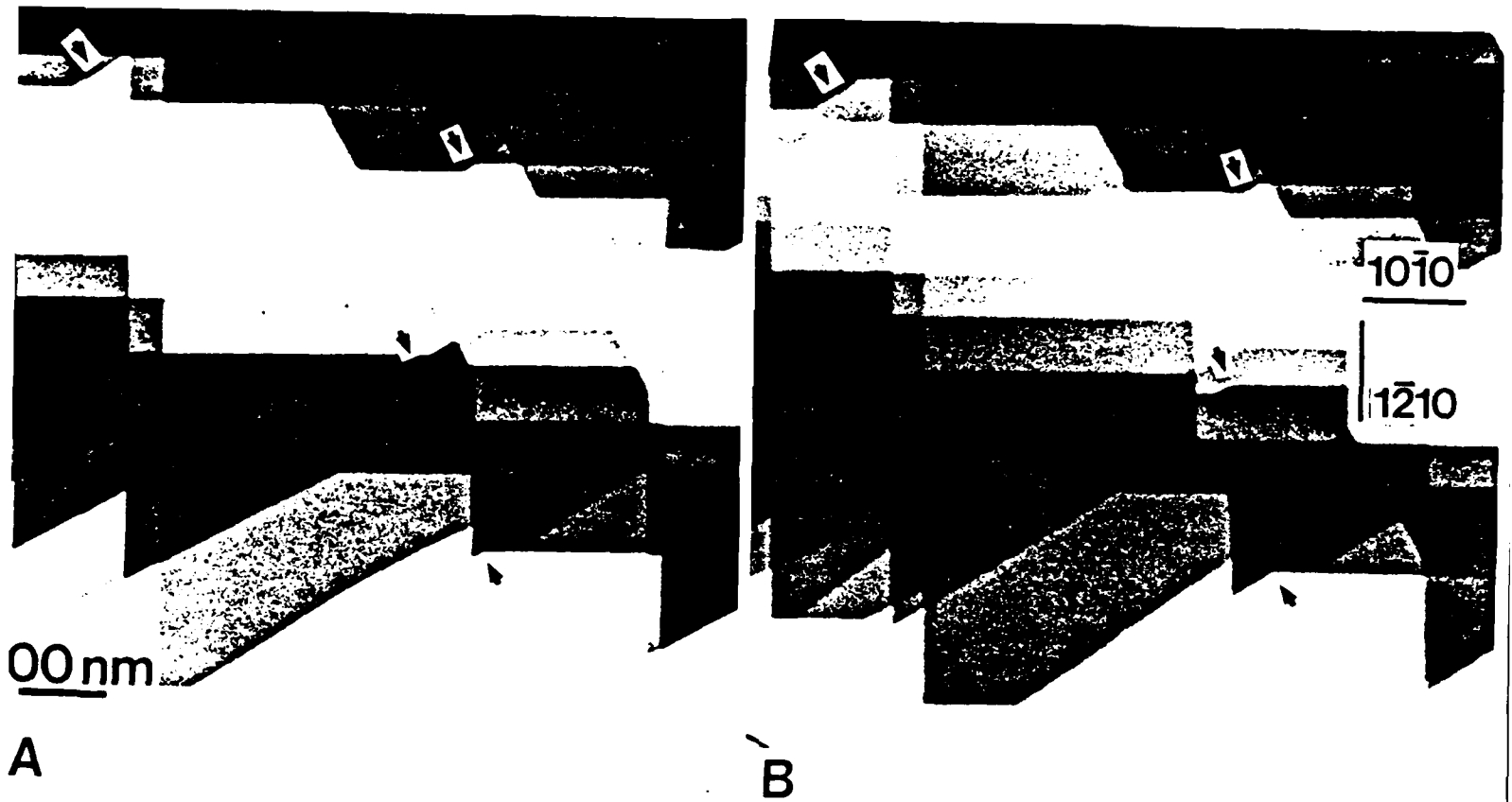


Fig.2 Step movement on (0001) α - Al_2O_3 surface. Same area of specimen shown A.) after 24h at 1400°C and B.) after a further heat treatment in air at 1200°C for 3h. C.) Schematic diagram of superposition of "A" and "B" with differences, or step movement, noted by dotted lines. Reference arrows are included for examining individual step kinks.

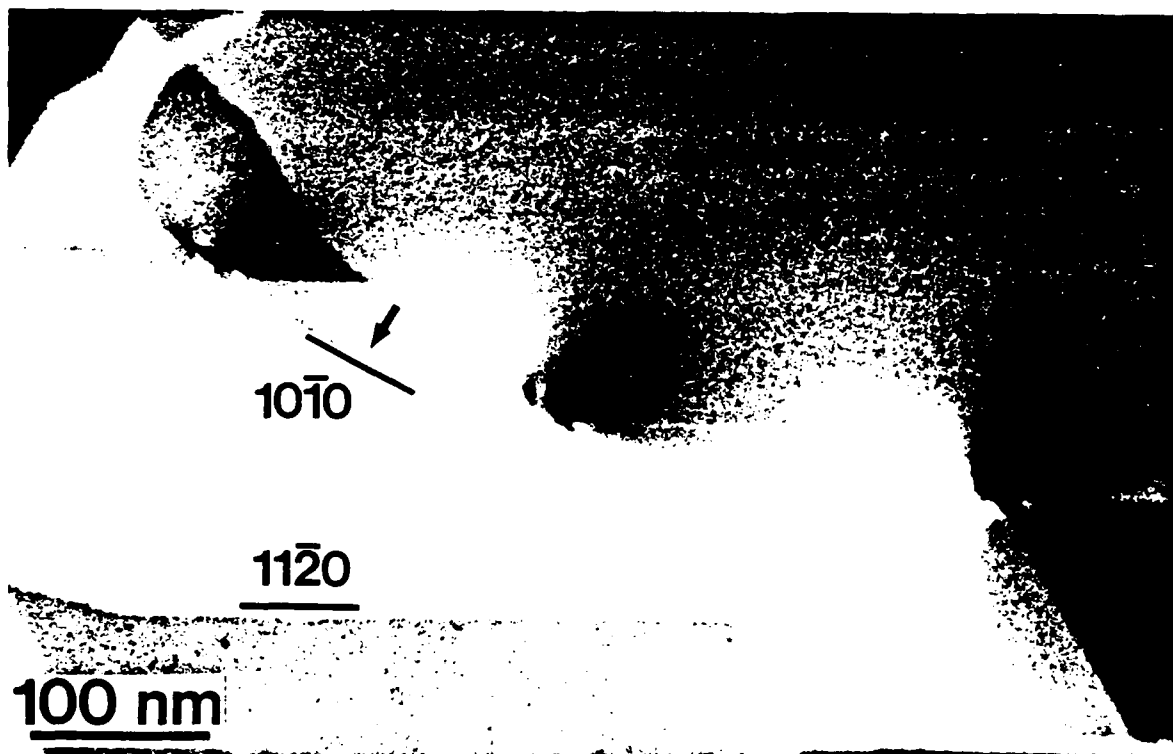


Fig.3 Step pinning at dislocations on (0001) -Al₂O₃ surface. Note that steps tend to bow out along low-index crystallographic planes.

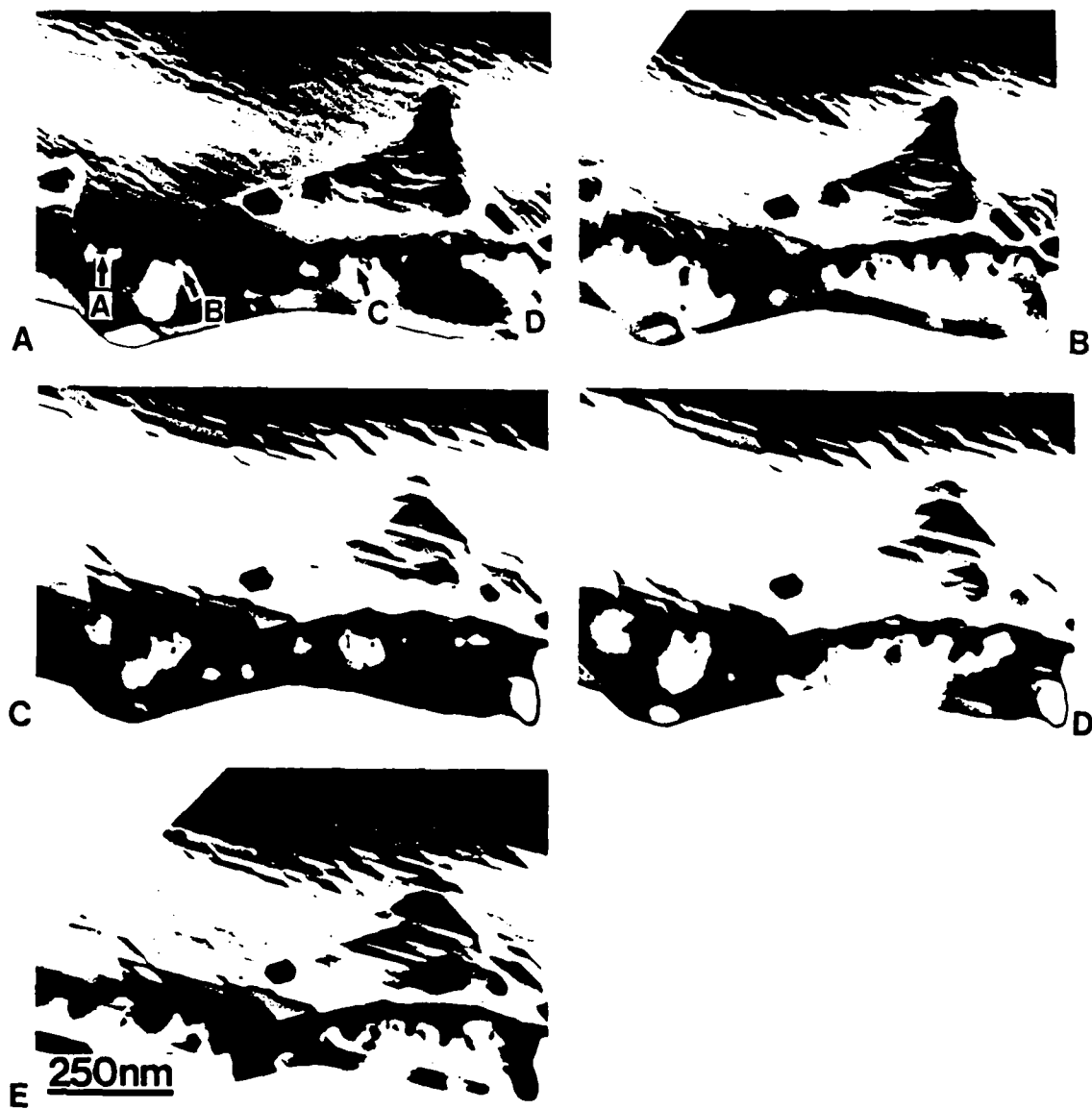


Fig.4 Step - dislocation interactions on (0001) α -Al₂O₃ surface during annealing sequence at 1200°C after A.) 10min, B.) 2h, C.) 4h, D.) 6h and E.) 8h.

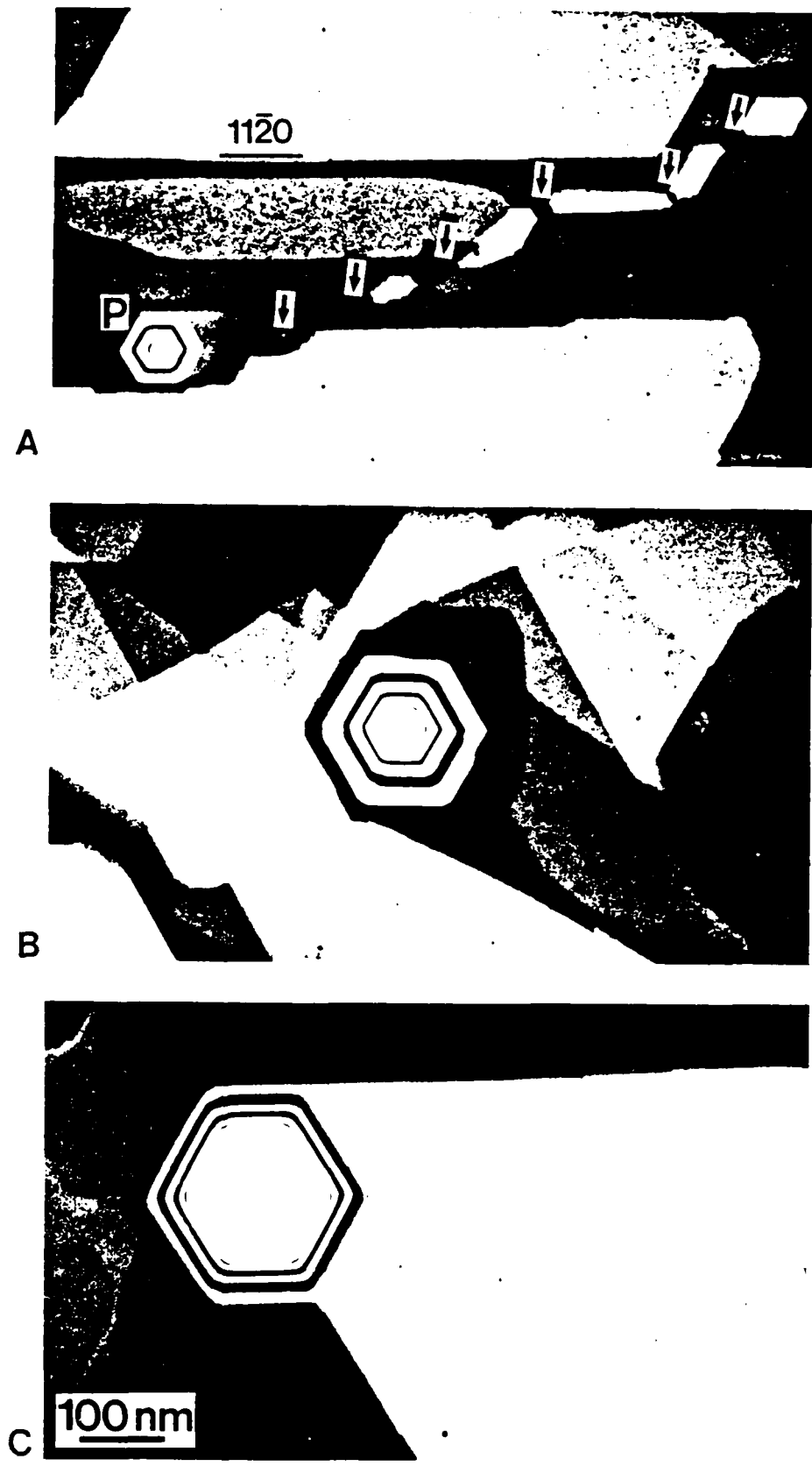


Fig.5 Thermal etch pits or "pores" formed in (0001) α - Al_2O_3 surface. A.) Pore is associated with row of dislocations (arrowed). B.) 50nm circular pore faceted on planes inclined to (0001). C.) 150nm pore showing pseudo-six fold symmetry and pinning surface steps.

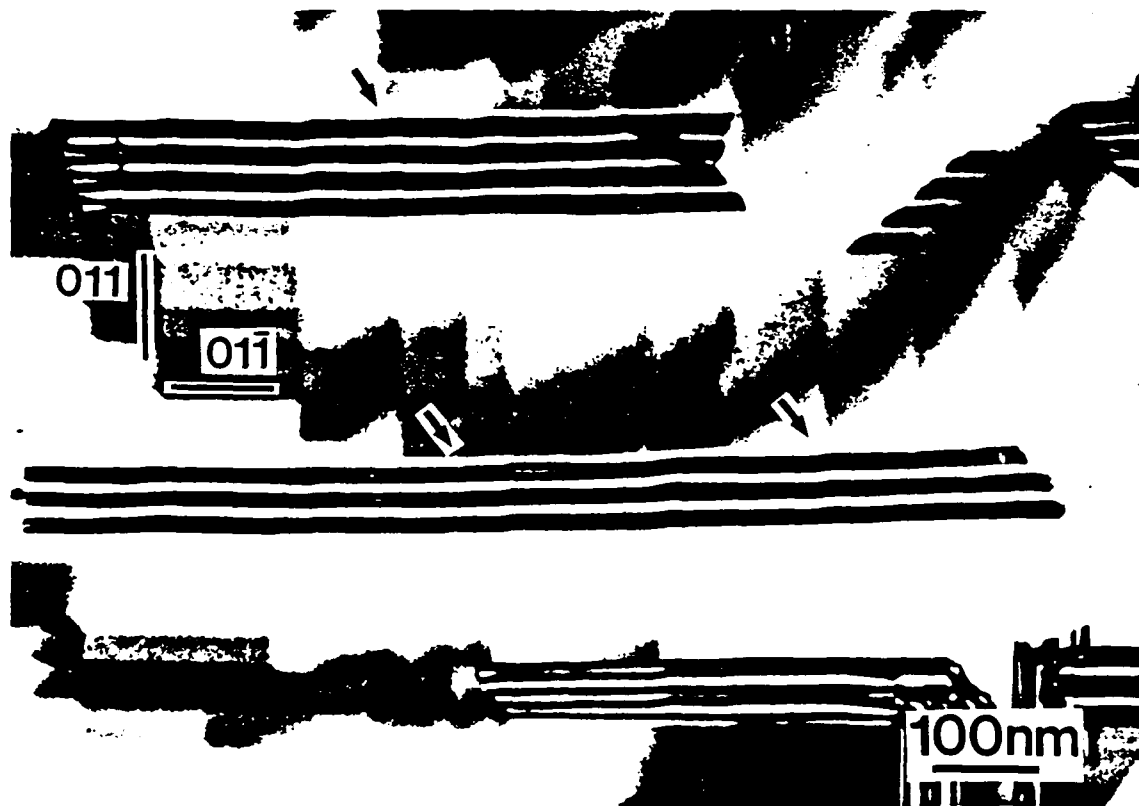


Fig.6 BF image of surface step / stacking fault intersections (arrowed, for example) on (100) β -0SiC.



Fig.7 Step / stacking fault intersections on (100) β -SiC. A.) BF image and B.) $(02\bar{2})$ and C.) (022) WBDF images. Note intersections (arrowed) and offsets (enlarged and arrowed in "D" and "E") that occur on one side of stacking fault only.

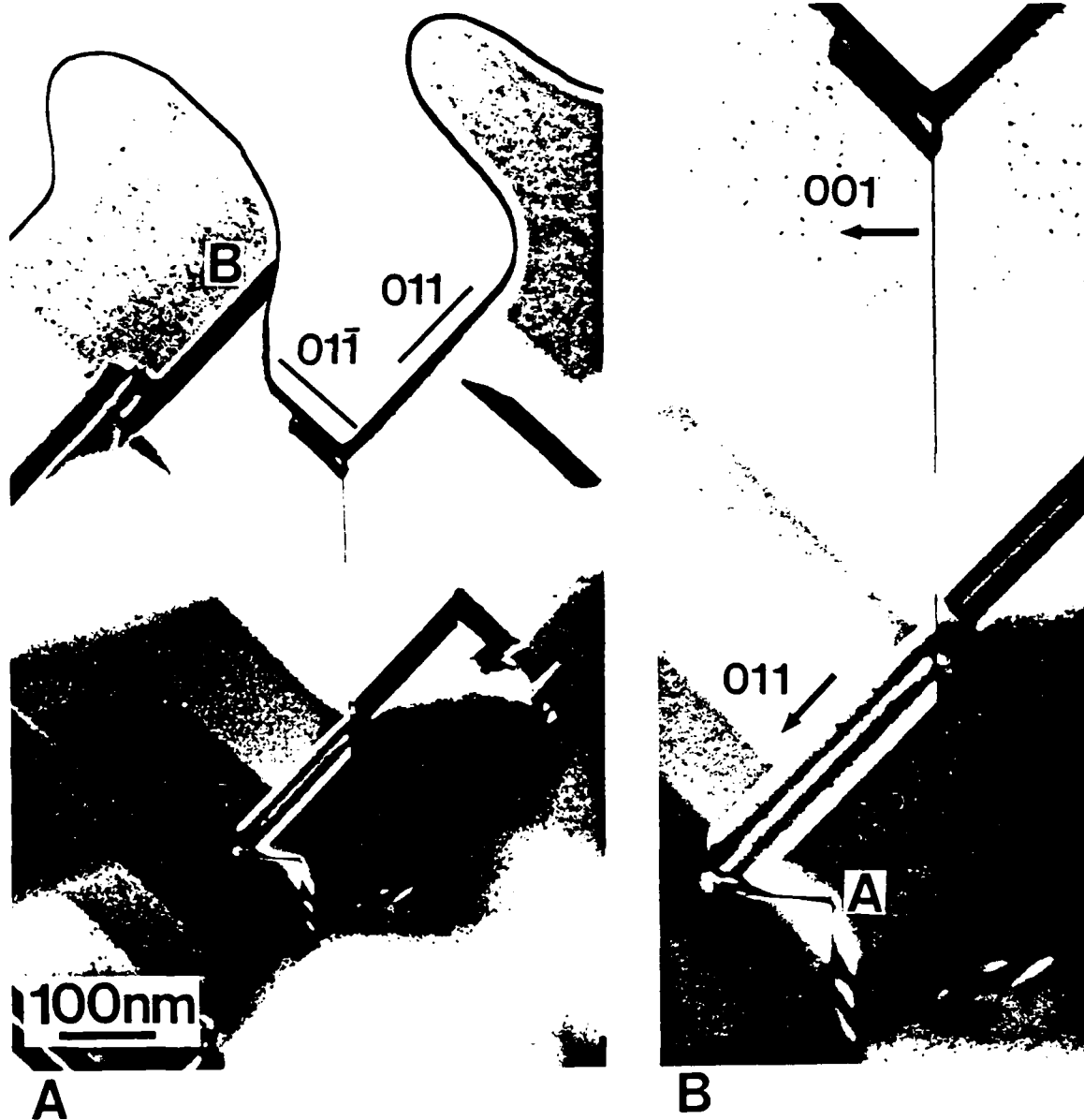


Fig.8 Thermal groove at intersection between APB and surface of (100) β -SiC. A.) Groove faceted on {011} planes. Note absence of groove at stacking fault labelled B. B.) Preferential thinning or grooving recorded from top and bottom surfaces as light-shaded material at A.

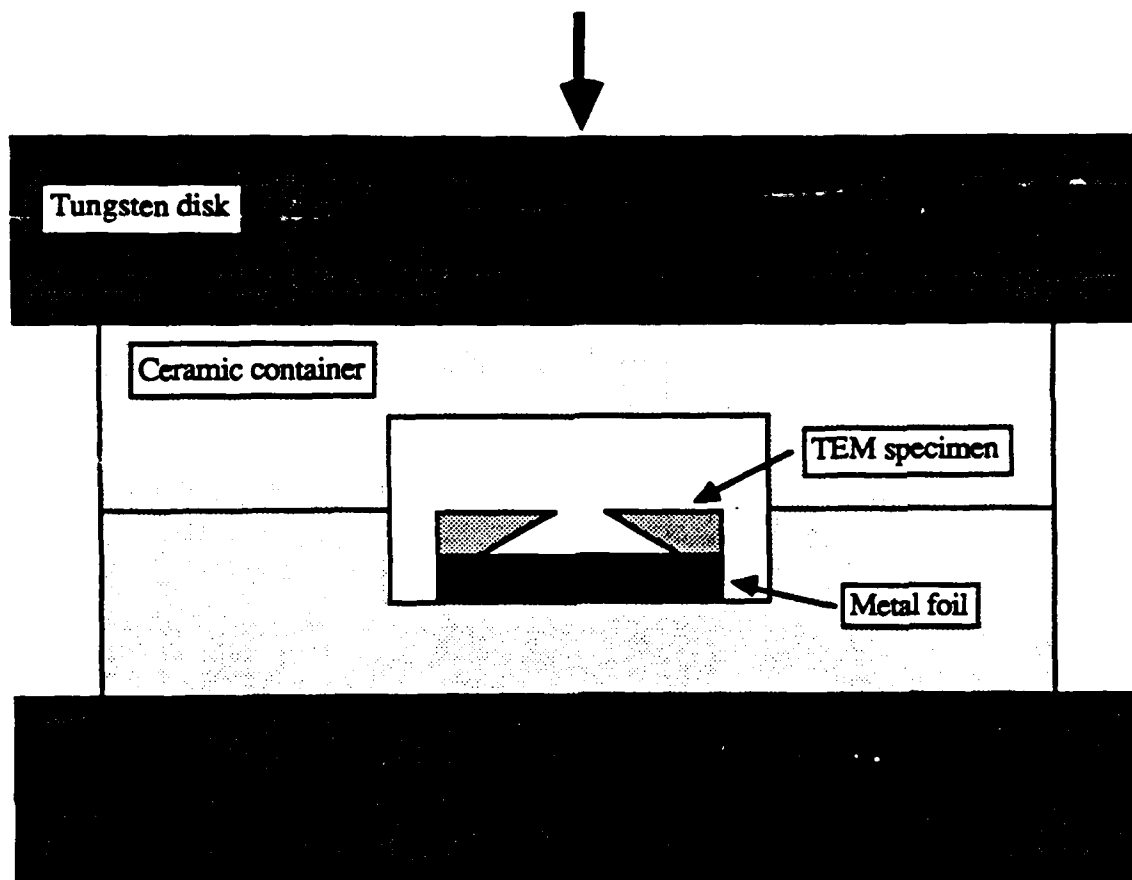
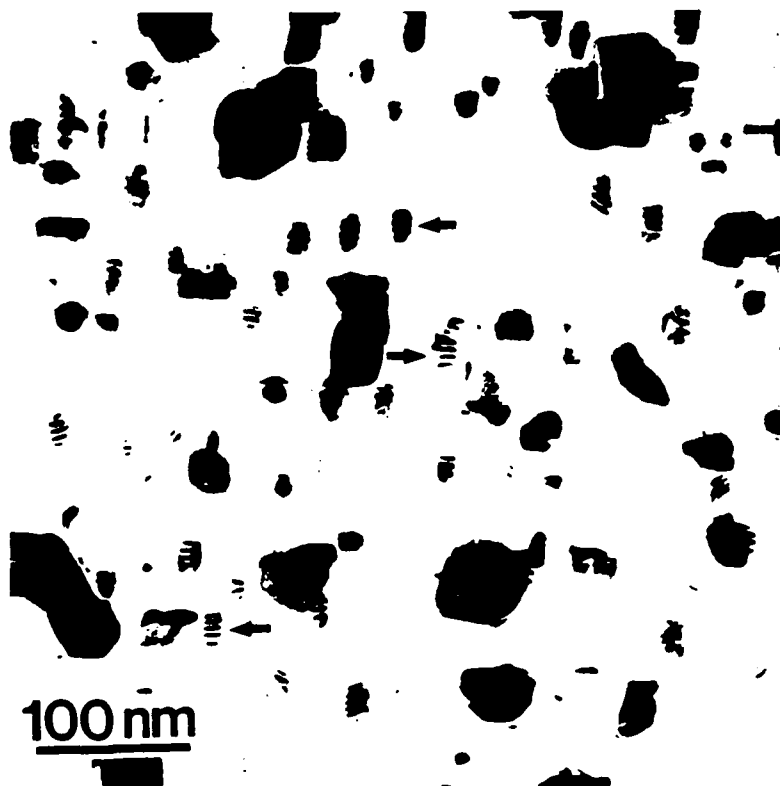
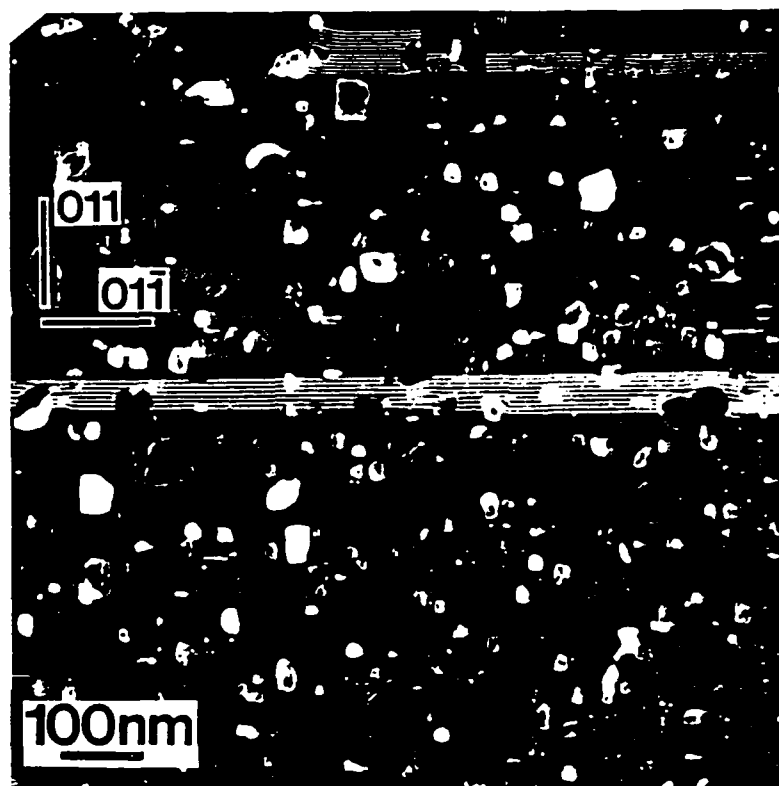


Fig.9 Schematic diagram of metal evaporation chamber. Perforated TEM specimen placed above metal foil and enclosed within ceramic container.

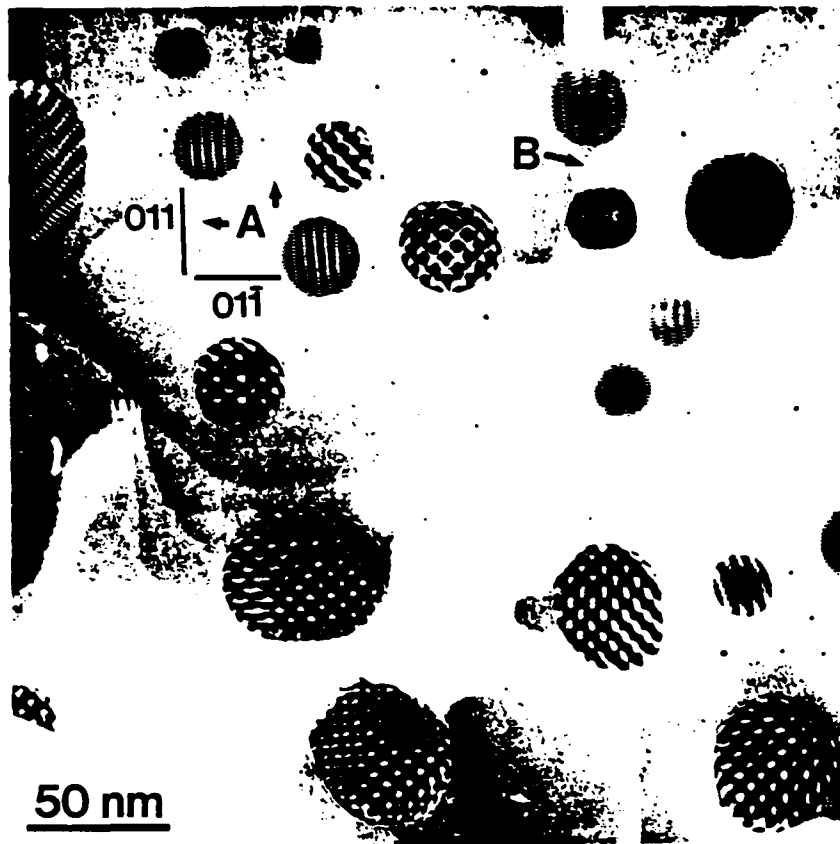


A



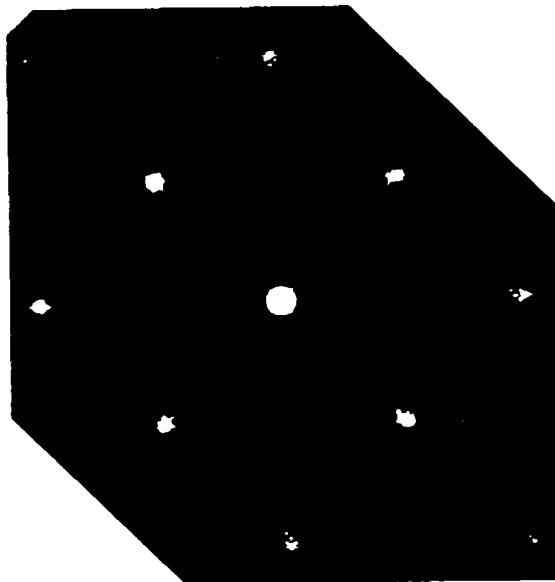
B

Fig.10 Tungsten particles on (100) β -SiC surface after 15min at 1200°C. A.) Moiré fringes (arrowed, for example) present in one direction in particles. Note absence of surface steps. B.) Centered-dark field image recorded with (022) β -SiC reflection with both stacking fault and tungsten particles illuminated.

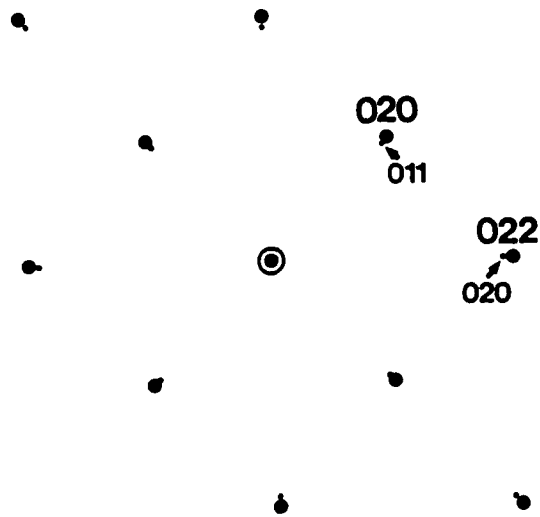


50 nm

A



B



C

Fig.11 Tungsten particles on (100) β -SiC surface after 1h at 1200°C. A.) BF image showing surface steps and tungsten particles with Moiré fringes in orthogonal directions and B.) corresponding SAD pattern and C.) schematic diagram illustrating orientation relation, $\{020\}_w \parallel \{022\}_{\beta\text{-SiC}}$ with $[100]_w \parallel [100]_{\beta\text{-SiC}}$.

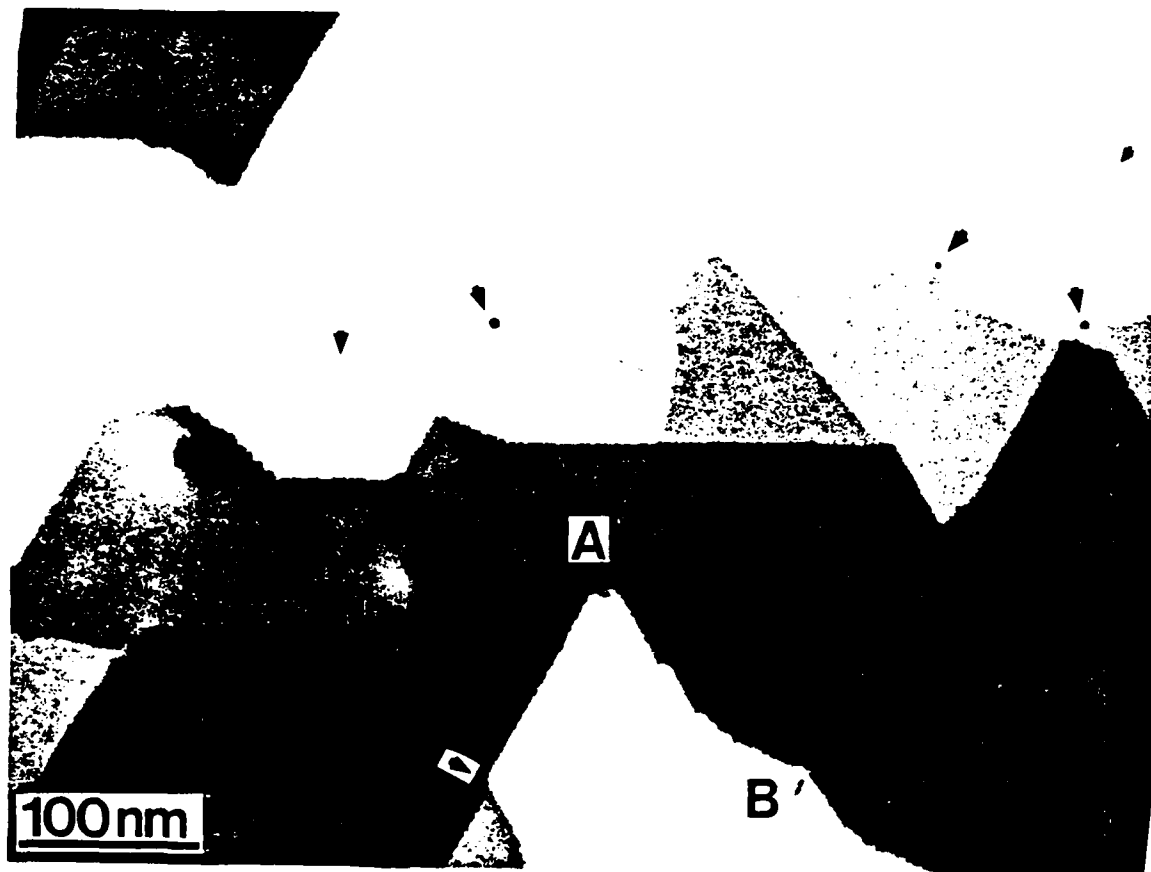
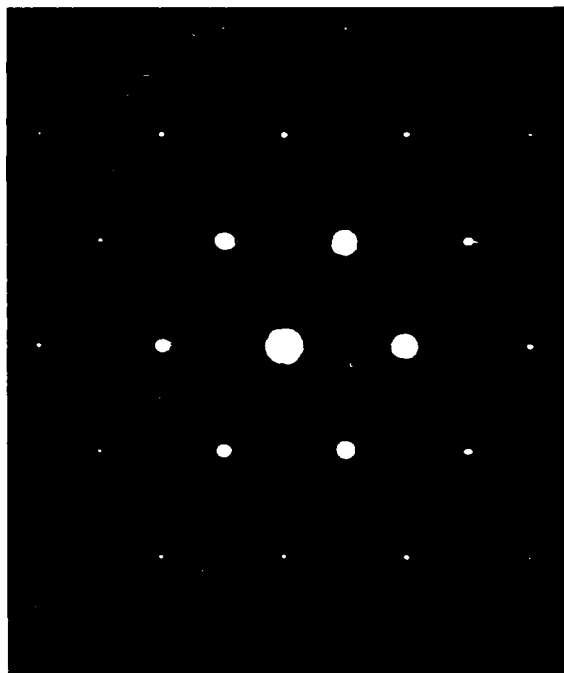
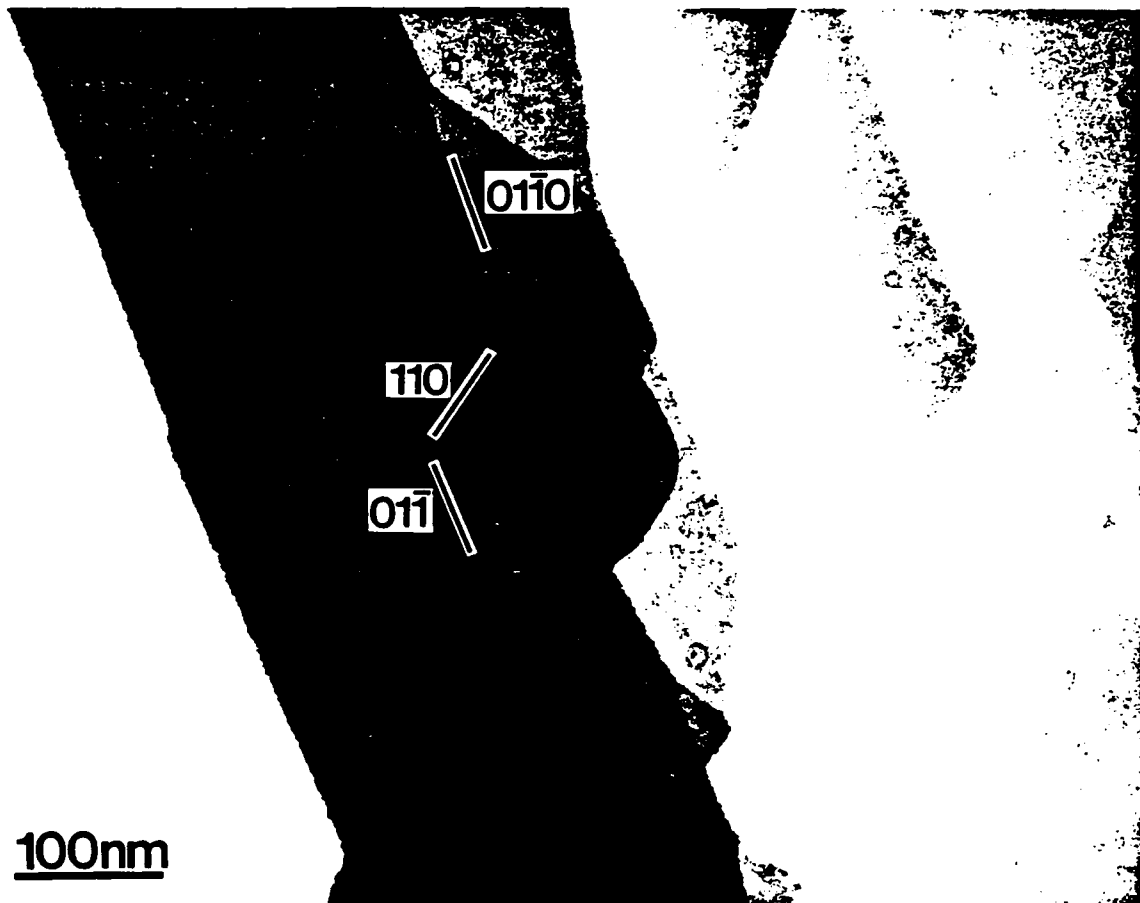


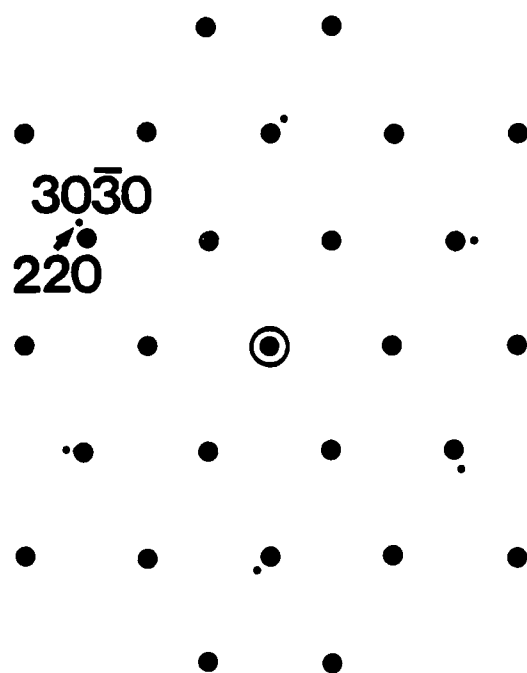
Fig.12 Small tungsten particles (arrowed) and dislocations (labelled at A and B) pinning steps on (0001) α - Al_2O_3 surface.



Fig. 13 Copper particles evaporated onto (0001) α - Al_2O_3 surface and generally associated with steps on the surface. A.) Low-magnification BF image of particle distribution and B.) four copper particles aligned to step on (11 $\bar{2}$ 0) plane.

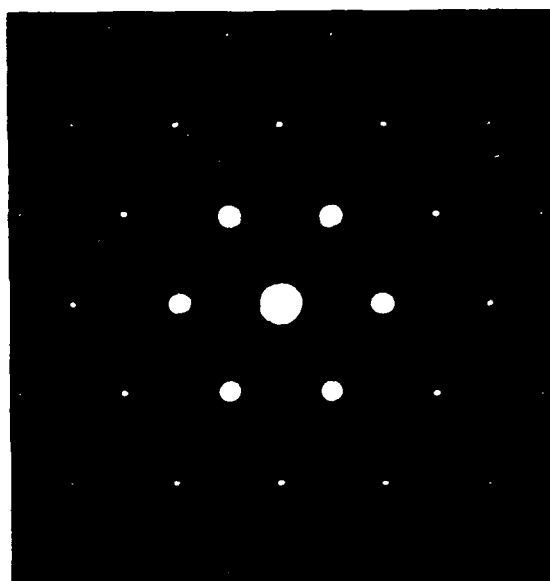
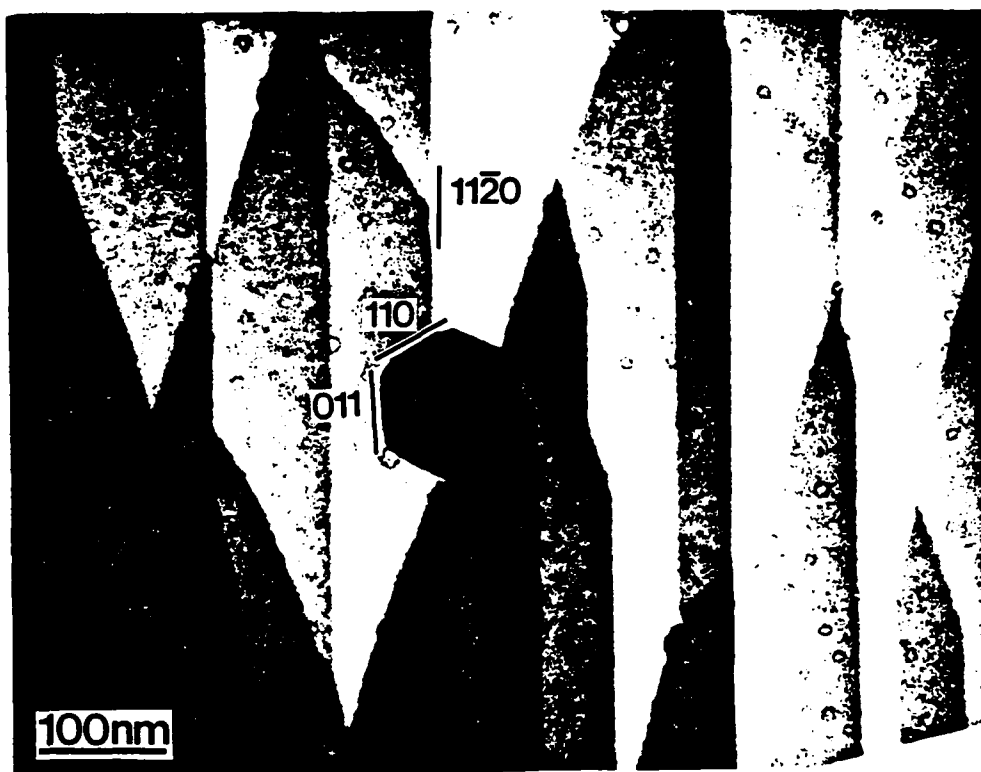


B

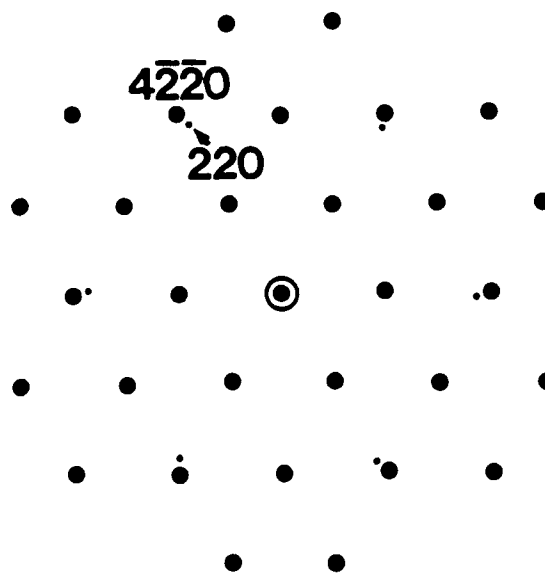


C

Fig.14 Copper particle on (0001) α - Al_2O_3 surface with $\{220\}_{\text{Cu}} \parallel \{30\bar{3}0\}_{\alpha\text{-Al}_2\text{O}_3}$. A.) BF image, B.) corresponding SAD pattern and C.) schematic diagram. Note that $\{220\}_{\text{Cu}}$ reflections are outside the $\{30\bar{3}0\}_{\alpha\text{-Al}_2\text{O}_3}$ reflections.

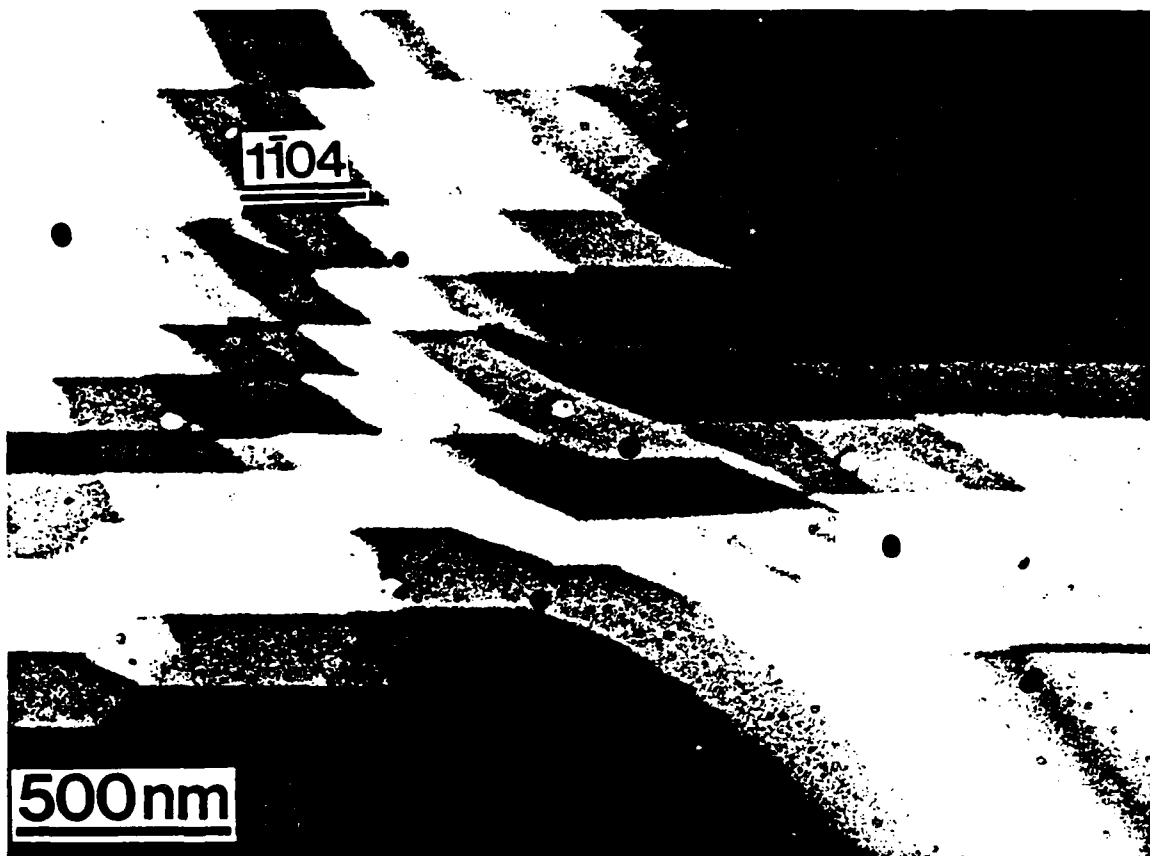


B

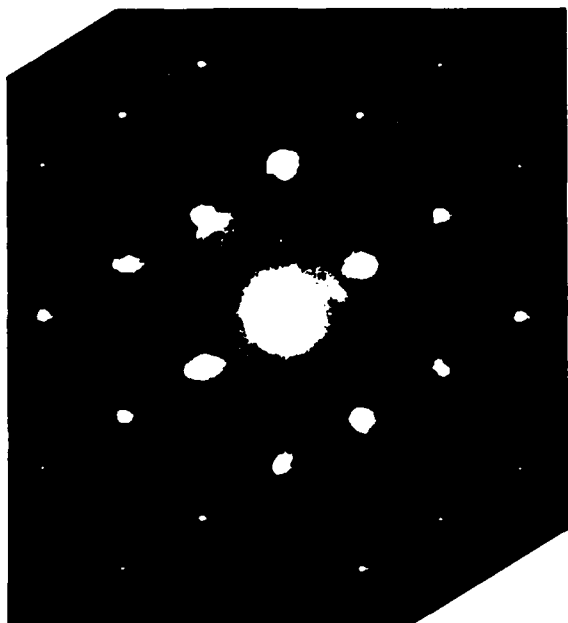


C

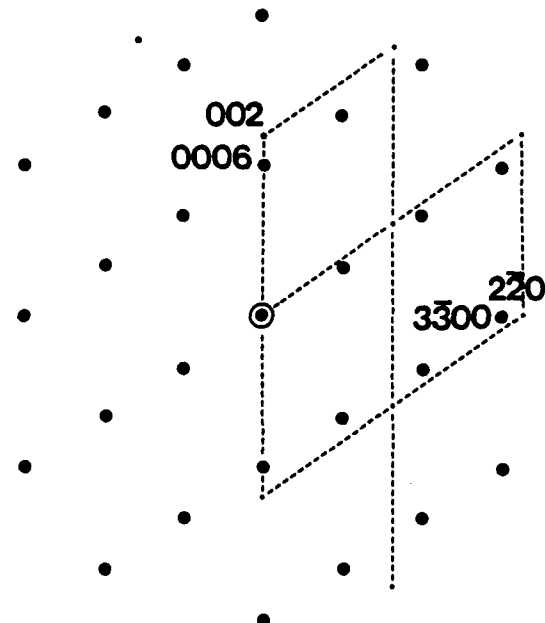
Fig.15 Copper particle on (0001) α - Al_2O_3 surface with $\{220\}_{\text{Cu}} \parallel \{22\bar{4}0\}_{\alpha\text{-Al}_2\text{O}_3}$. A.) BF image, B.) corresponding SAD pattern and C.) schematic diagram. Note that $\{220\}_{\text{Cu}}$ reflections are inside the $\{22\bar{4}0\}_{\alpha\text{-Al}_2\text{O}_3}$ reflections.



A



B



C

Fig.16 A.) Low-magnification BF image of copper particles on $(11\bar{0}0)$ α - Al_2O_3 surface, B.) SAD pattern and C.) schematic diagram of orientation relation, $(002)\text{Cu} \parallel (0006)\text{Al}_2\text{O}_3$ and $(2\bar{2}0)\text{Cu} \parallel (3\bar{3}00)\text{Al}_2\text{O}_3$ with $[110]\text{Cu} \parallel [11\bar{2}0]\text{Al}_2\text{O}_3$.

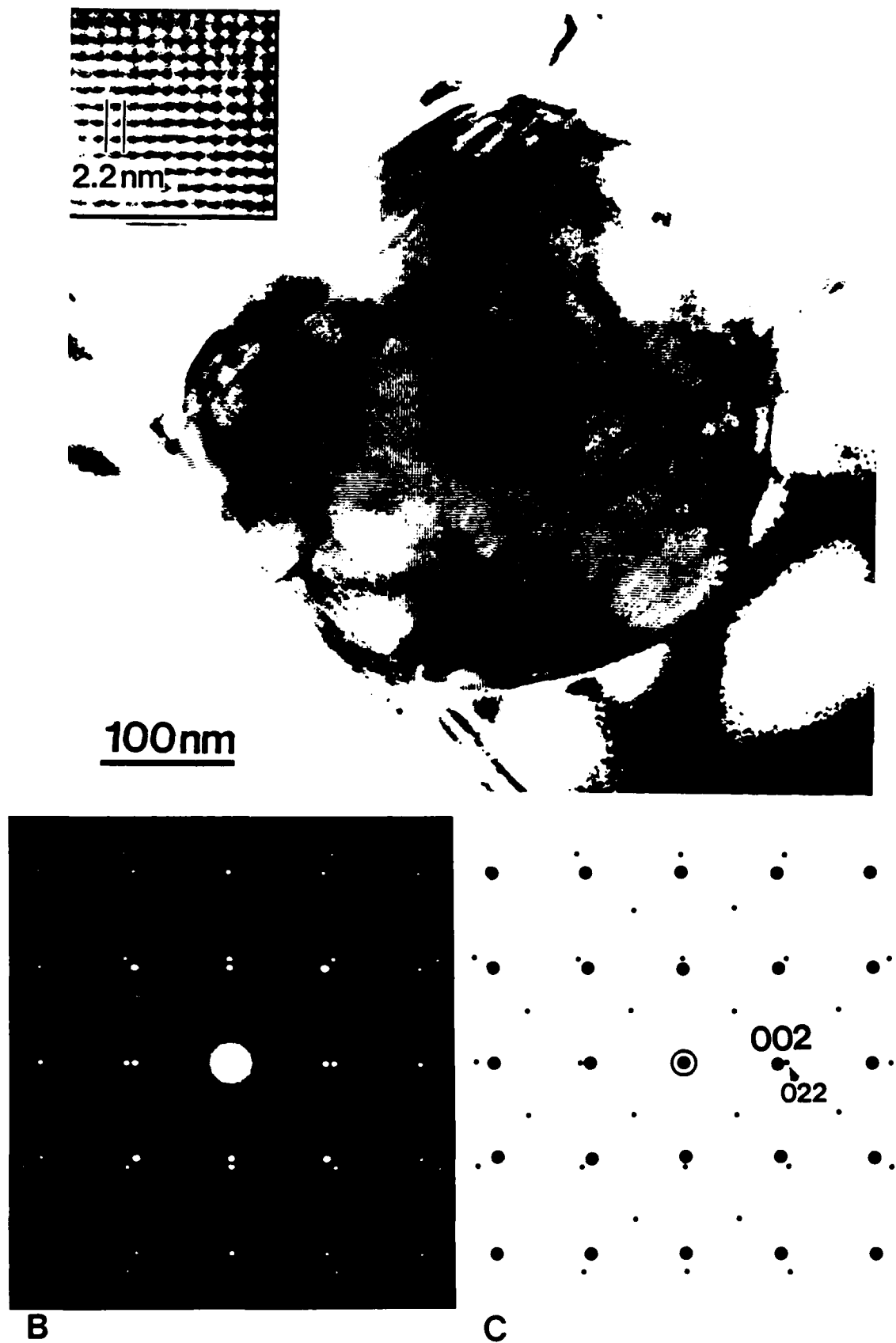


Fig.17 ThO₂ particle on (100) β-SiC surface. A.) BF image , B.) corresponding SAD pattern and C.) schematic diagram which shows (002)_{β-SiC} || (022)_{ThO₂} with [100]_{β-SiC} || [100]_{ThO₂}. Moiré fringe periodicity in "A" (2.16nm) consistent with 9.3% lattice misfit.

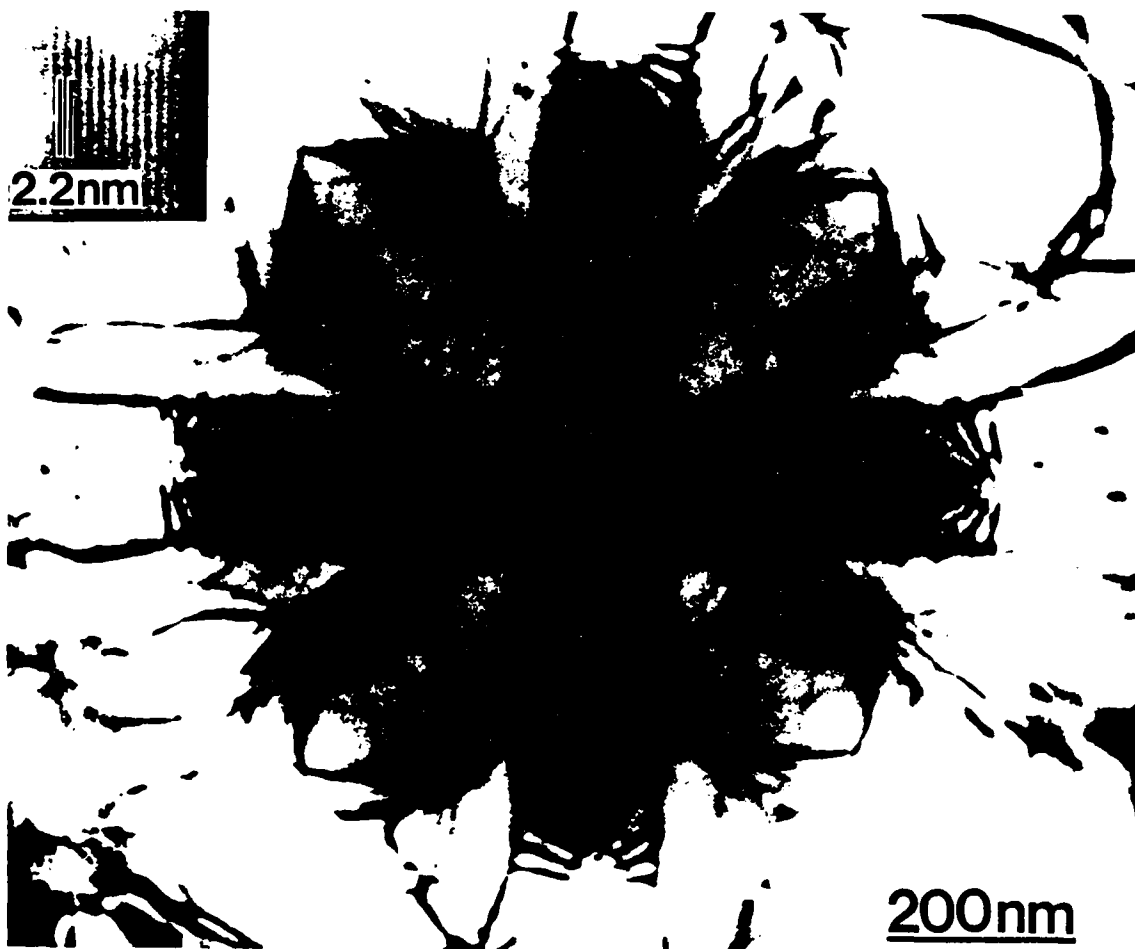


Fig.18 1 μ m-size ThO₂ particle on (100) β -SiC showing four-fold bend contour pattern in ThO₂ particle and bending in substrate in $\langle 010 \rangle$ directions.

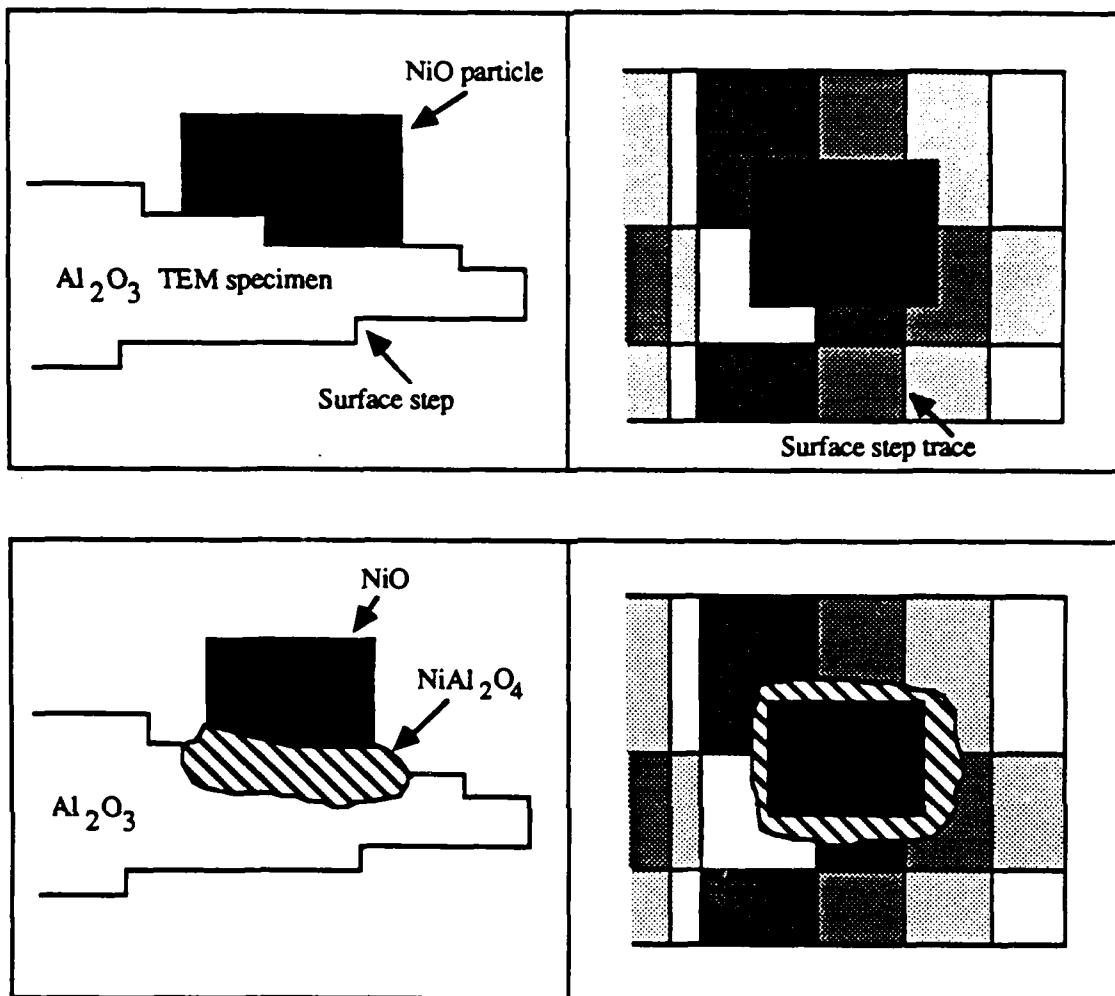


Fig.19 Schematic illustration of thin-film reaction couple with NiO particle deposited onto faceted surface of annealed α - Al_2O_3 TEM specimen A.) in cross section and B.) in plan view. NiAl_2O_4 layer forms during subsequent annealing and is shown in "C" and "D".

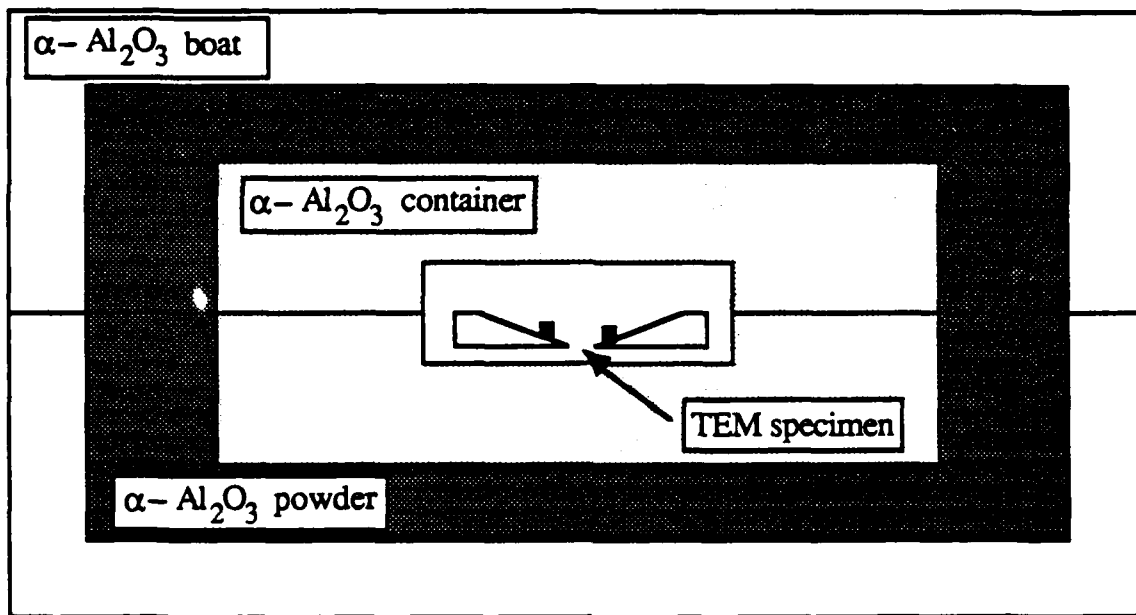


Fig.20 Schematic illustration of assembly used for annealing thin-film reaction couple. TEM specimen is placed in single-crystal $\alpha\text{-Al}_2\text{O}_3$ container, surrounded by high-purity $\alpha\text{-Al}_2\text{O}_3$ powder and enclosed within $\alpha\text{-Al}_2\text{O}_3$ furnace boats.

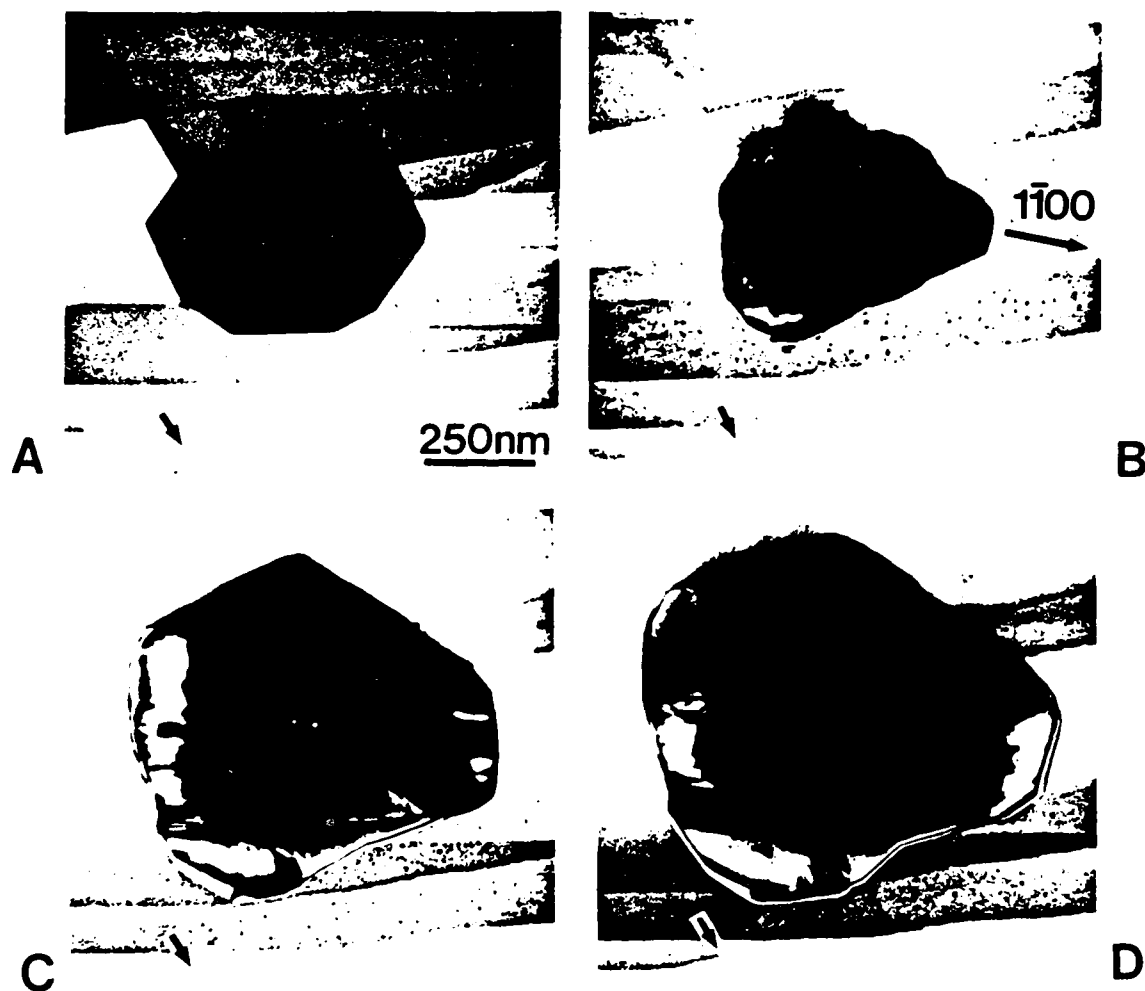


Fig.21 BF images of NiO particle on (0001) α -Al₂O₃ surface. A.) As deposited and after B.) 1h at 1120°C, C.) 1h at 1200°C and D.) 2h at 1200°C during which NiAl₂O₄ layer formed. Arrows indicate same step trace in each image.

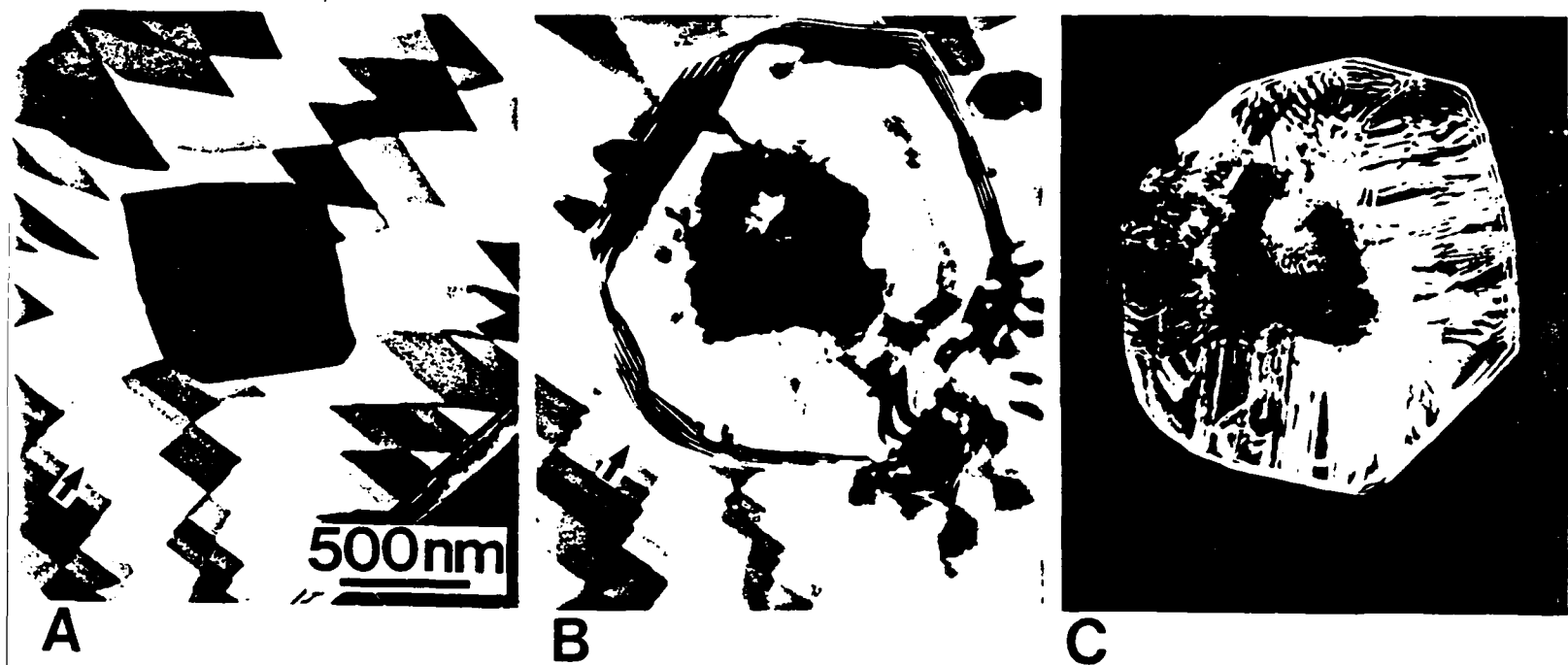


Fig.22 BF images of NiO particle on (0001) α -Al₂O₃ surface A.) as deposited and B.) after 1h at 1200°C during which NiAl₂O₄ layer formed. C.) (220)_{NiAl₂O₄} CDF image showing stacking faults and other defects within NiAl₂O₄ layer.

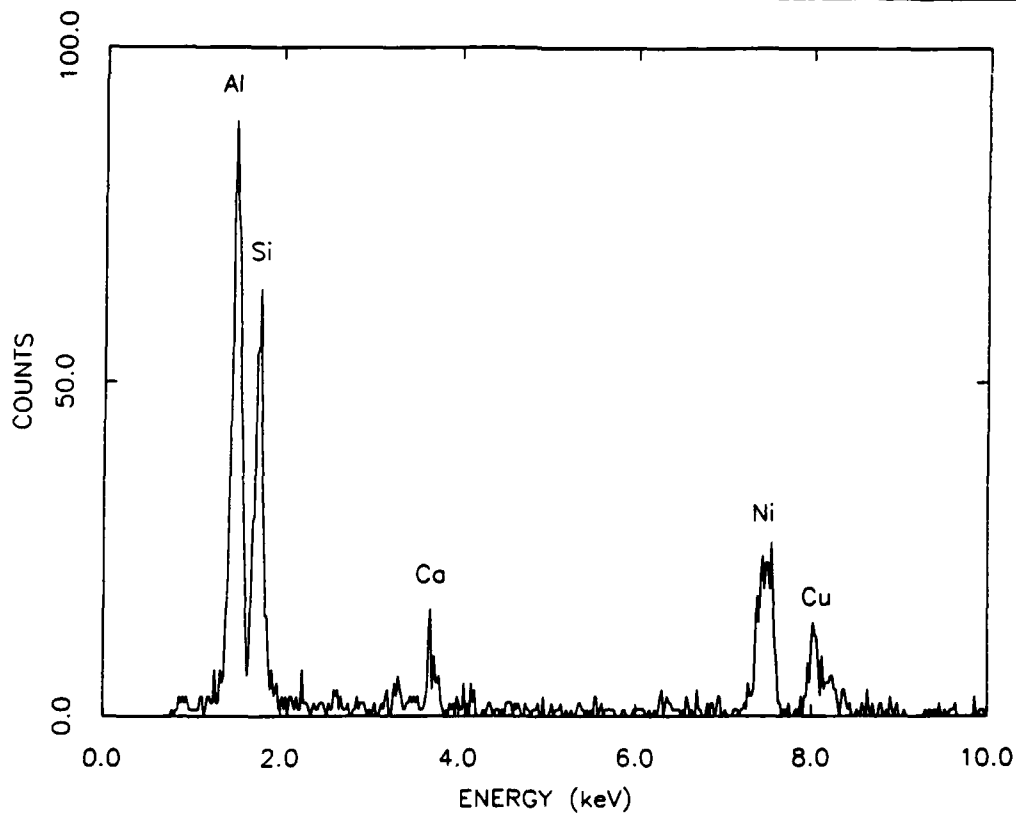
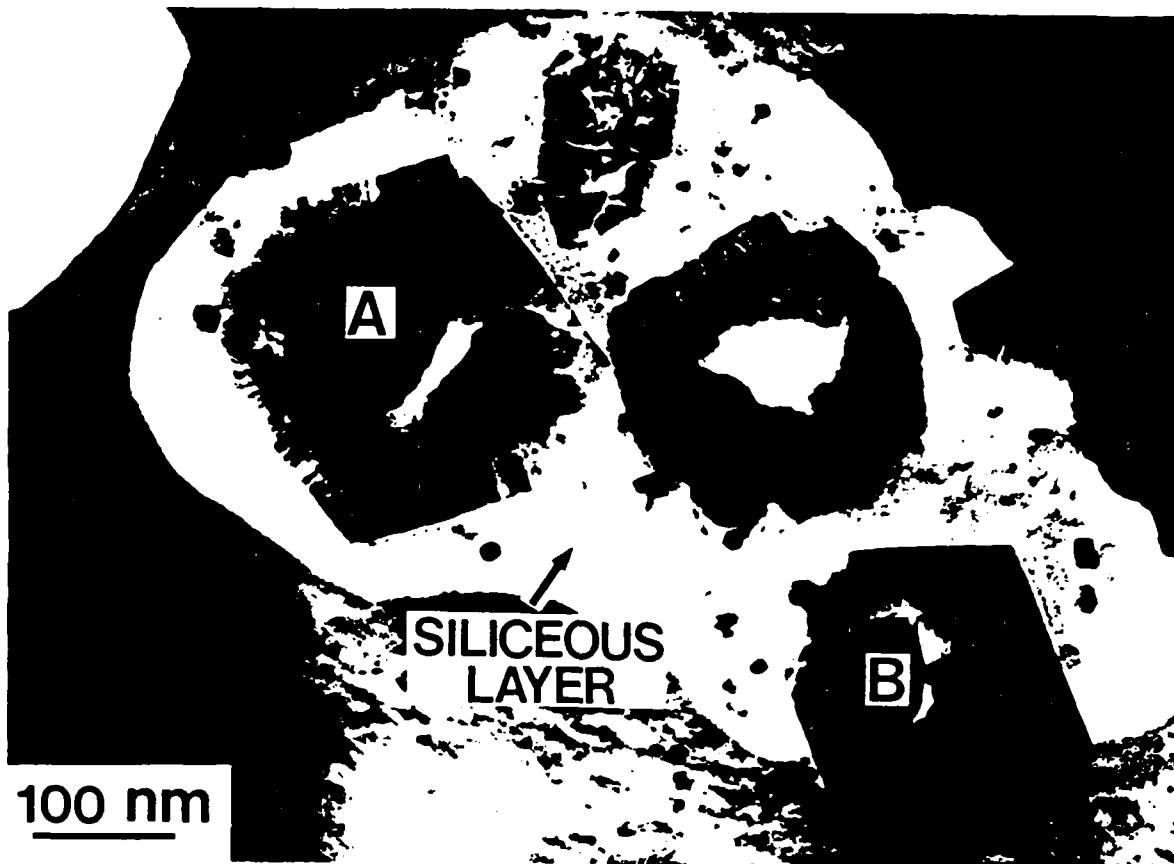


Fig.23 Contaminated thin-film reaction couple. A.) BF image showing light-shaded siliceous layer between NiAl_2O_4 particles and $\alpha\text{-Al}_2\text{O}_3$ substrate, B.) EDS spectrum recorded from contamination layer showing presence of Si and Ca impurities.

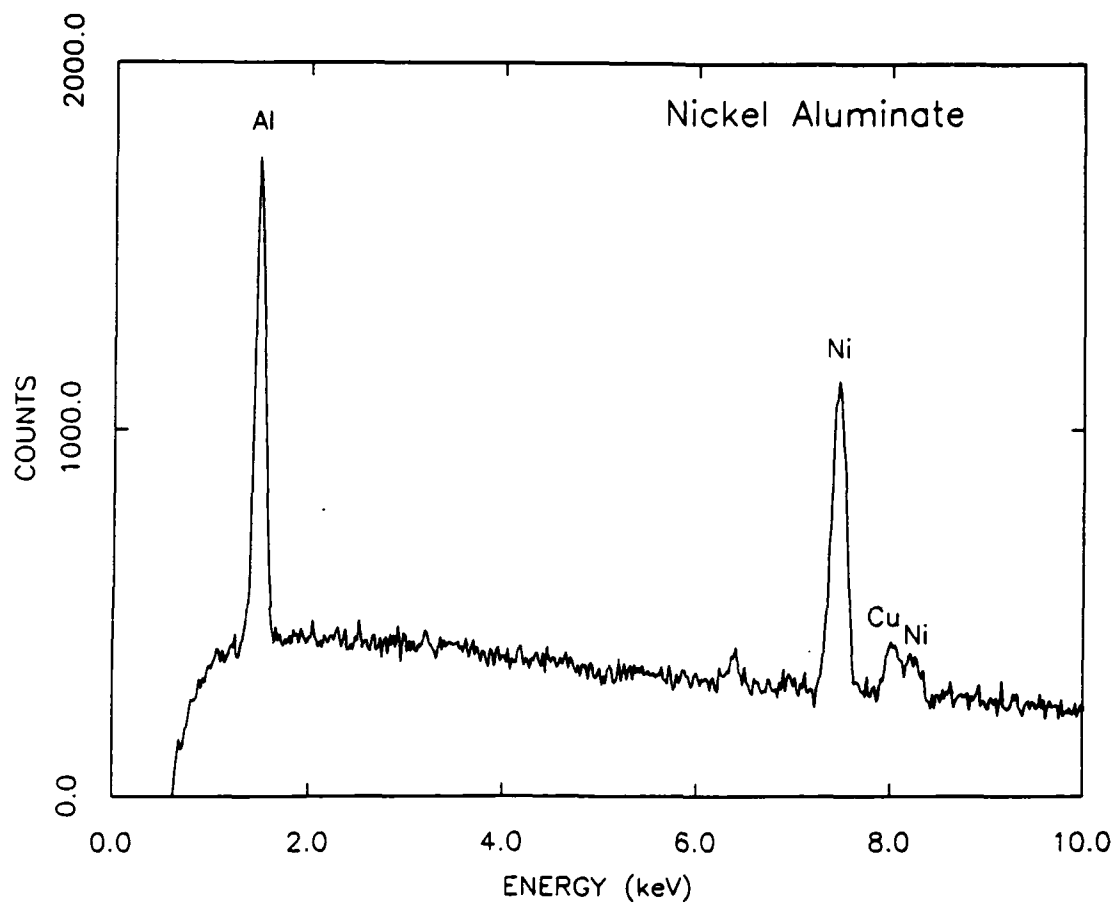


Fig.24 EDS spectrum from NiAl_2O_4 layer not contaminated with furnace impurities.

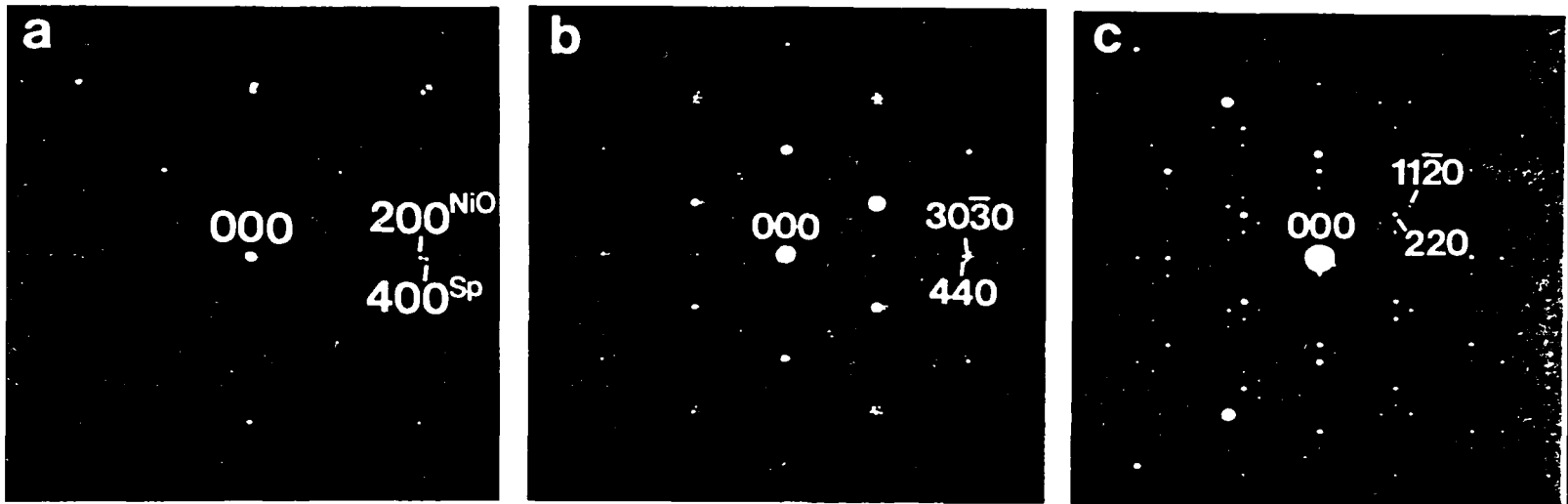


Fig.25 SAD patterns recorded from interfaces with special orientation relations. A.) $\{100\}_{\text{NiO}} \parallel \{100\}_{\text{NiAl}_2\text{O}_4}$, B.) $(440)_{\text{NiAl}_2\text{O}_4} \parallel (30\bar{3}0)_{\text{Al}_2\text{O}_3}$ with $[1\bar{1}1]_{\text{NiAl}_2\text{O}_4} \parallel [0001]_{\text{Al}_2\text{O}_3}$ and C.) $(220)_{\text{NiAl}_2\text{O}_4} \parallel (11\bar{2}0)_{\text{Al}_2\text{O}_3}$ with $[111]_{\text{NiAl}_2\text{O}_4} \parallel [0001]_{\text{Al}_2\text{O}_3}$.

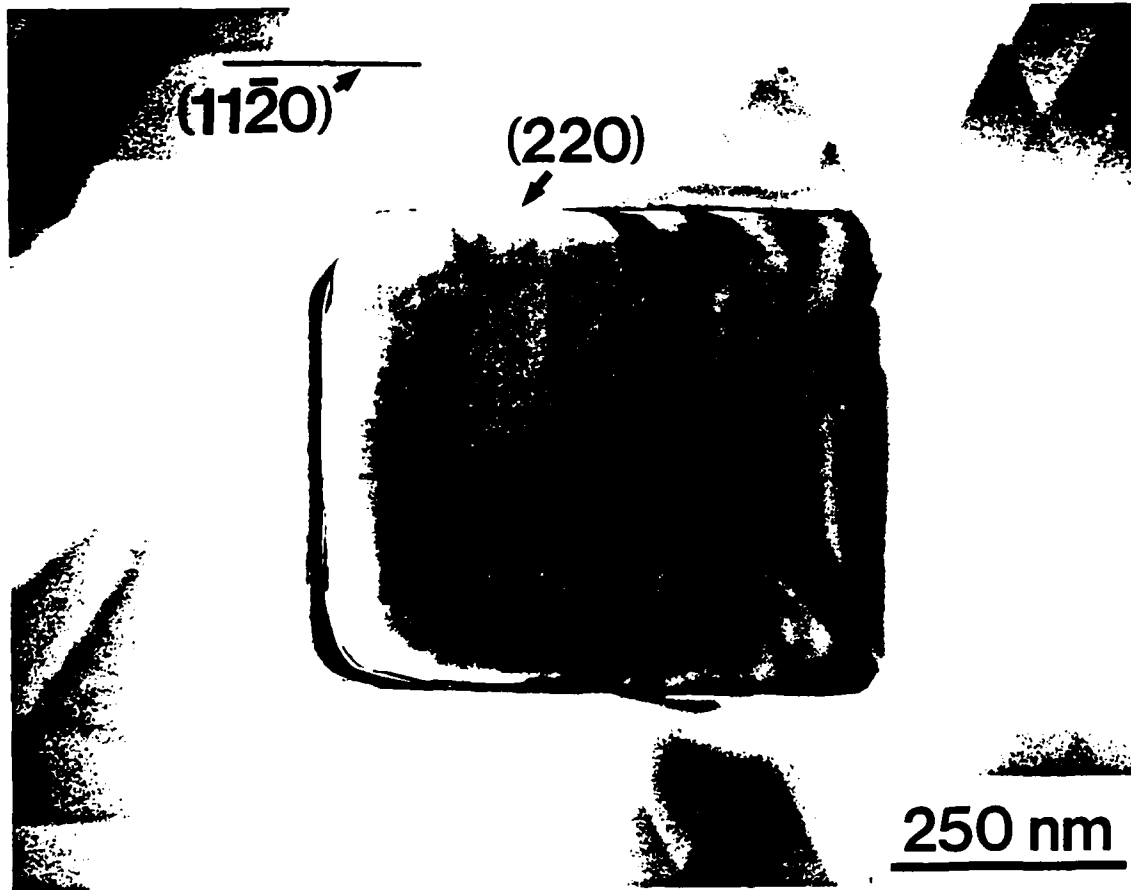


Fig.26 BF image form fully reacted NiO particle which developed facets parallel to step traces on α -Al₂O₃ surface.

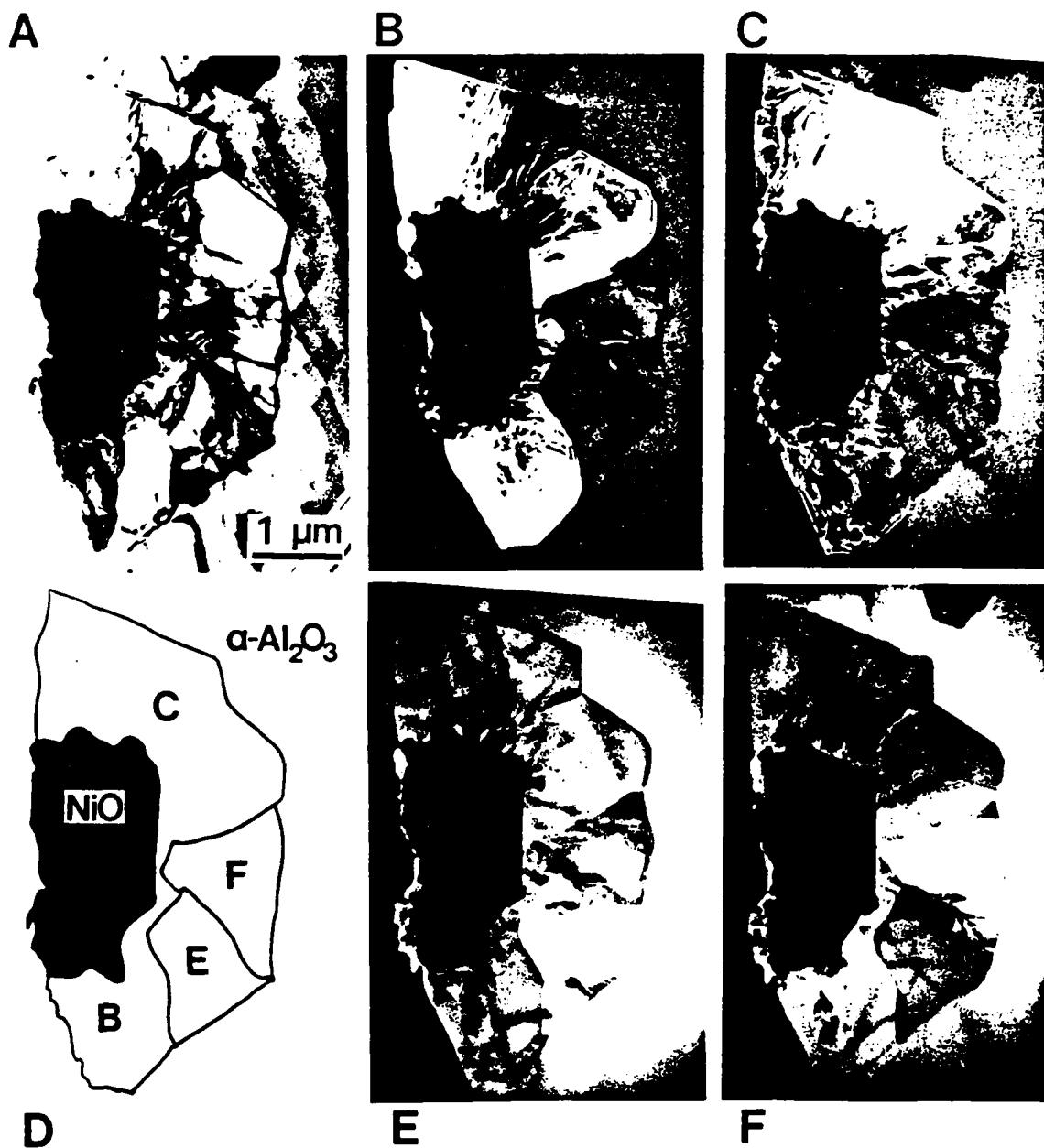


Fig.27 A.) BF image of NiO particles reacted with (0001) α -Al₂O₃ for 3h at 1200°C and B.) corresponding schematic diagram with domains of NiAl₂O₄ outlined. C,D.) (220)_{NiAl₂O₄} CDF images recorded from NiAl₂O₄ domains in contact with NiO. E,F.) (202)_{NiAl₂O₄} CDF images recorded from NiAl₂O₄ domains in contact with α -Al₂O₃ only.

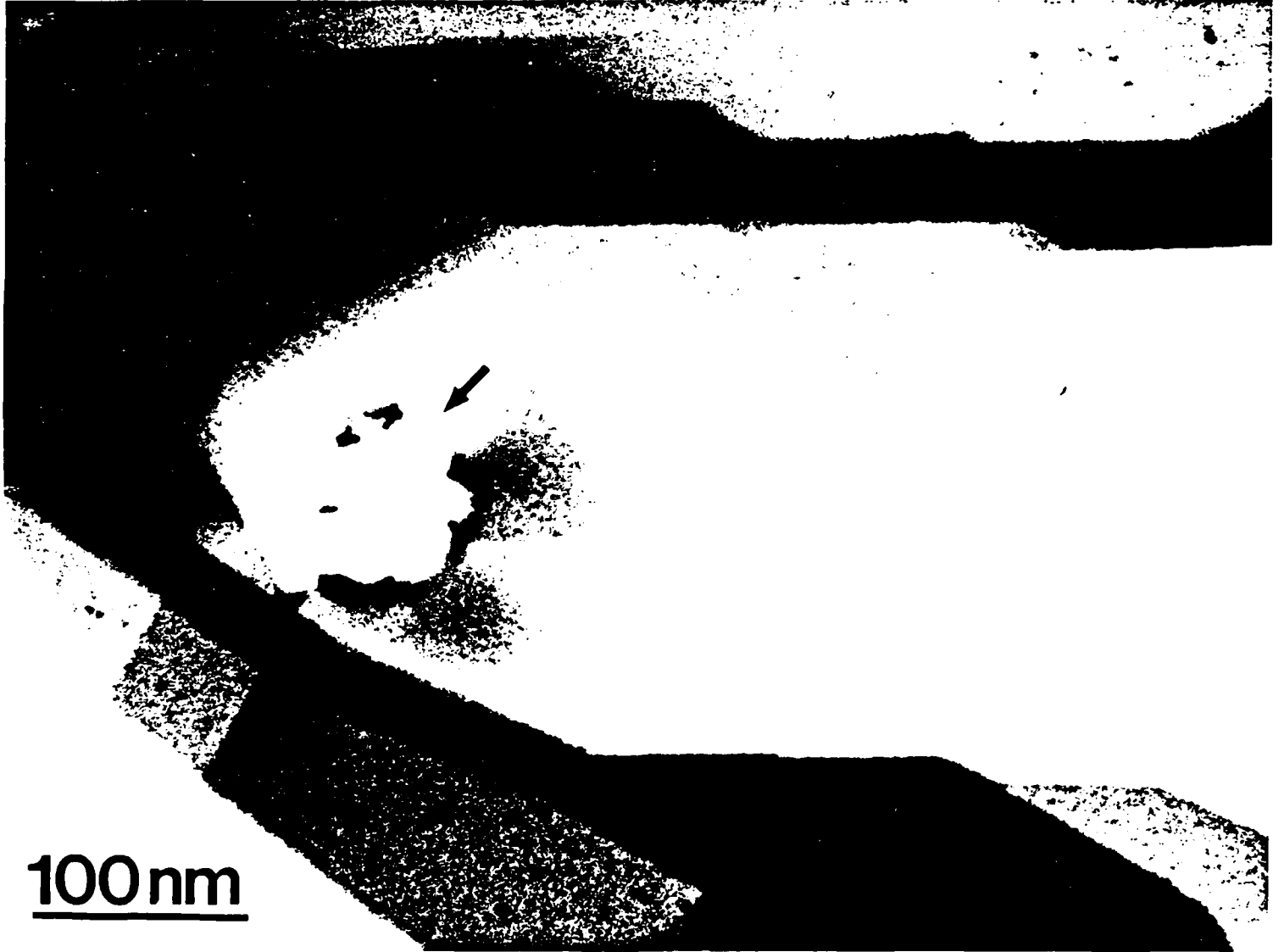


Fig.28 BF image of dislocation cluster circling thinned area on (0001) α -Al₂O₃ surface.

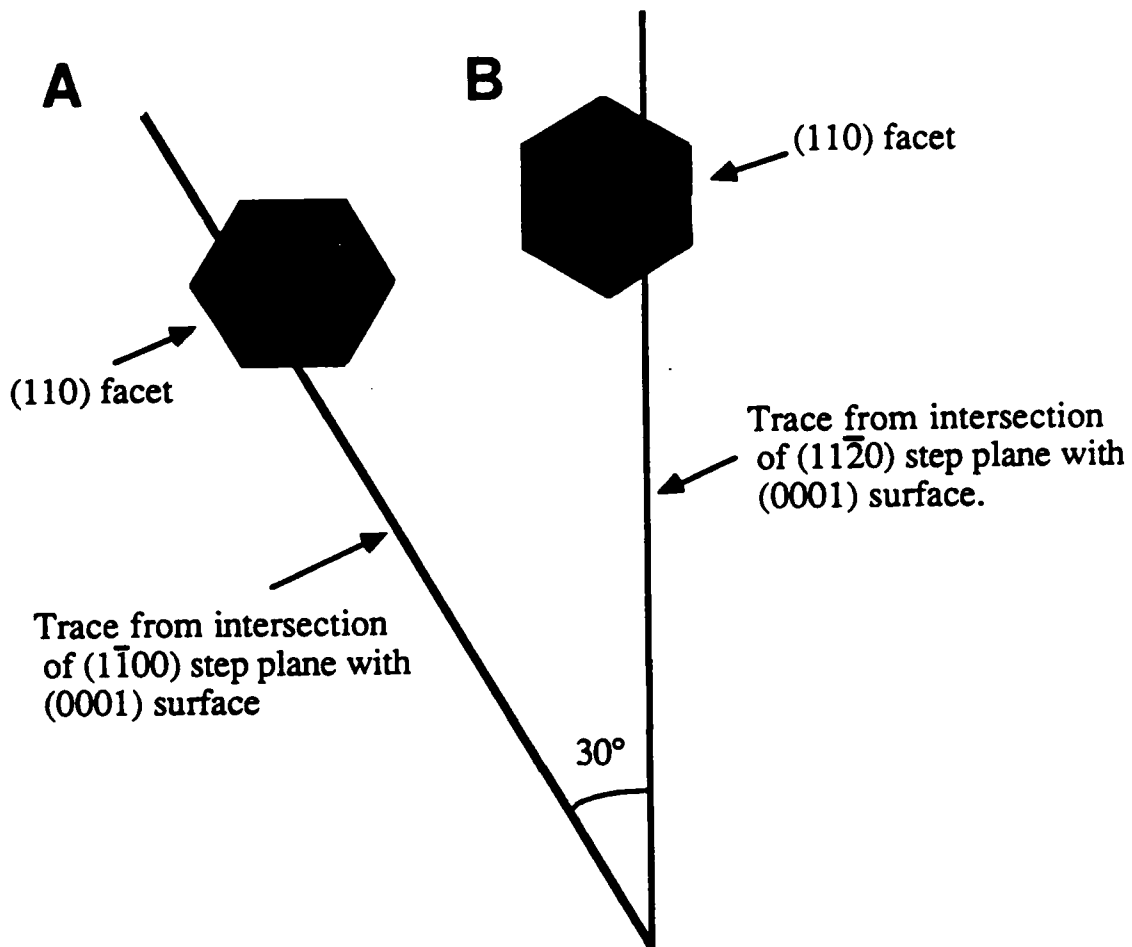


Fig.29 Schematic illustration of graphoepitaxy between faceted Cu particles and faceted (0001) $\alpha\text{-Al}_2\text{O}_3$ surface. A.) $(110)_{\text{Cu}}$ facet parallel to $(1\bar{1}00)_{\alpha\text{-Al}_2\text{O}_3}$ step trace and B.) $(110)_{\text{Cu}}$ facet parallel to $(11\bar{2}0)_{\alpha\text{-Al}_2\text{O}_3}$ step trace.

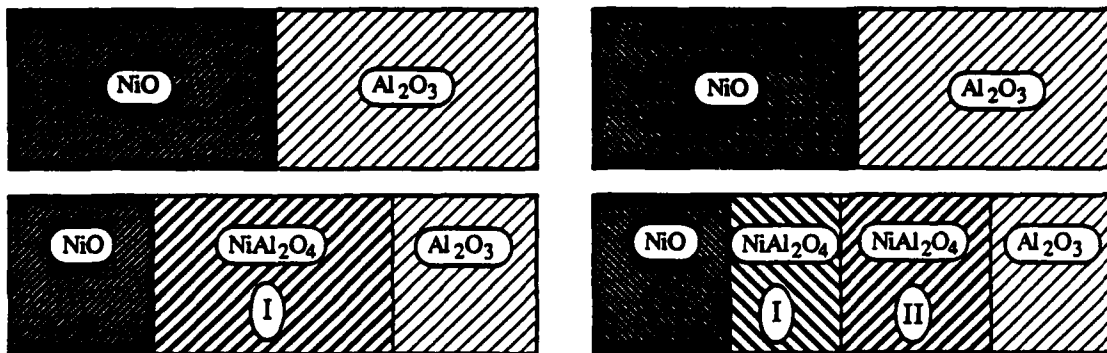


Fig.30 Schematic illustrations of possible reaction-couple geometries. A.) NiO is oriented to α -Al₂O₃ (denoted by continuous lines across NiO/ α -Al₂O₃ interface) from which B.) one layer of NiAl₂O₄ forms. C.) NiO not oriented to α -Al₂O₃ (discontinuity at NiO/ α -Al₂O₃ interface) and D.) two layers of NiAl₂O₄ form, I in registry with NiO and II in registry with α -Al₂O₃.